NTNU – Trondheim
Norwegian University of
Science and Technology

Photoelectrochemical Hydrogen Production

Marthe Emelie Melandsø Buan

Chemical Engineering and Biotechnology
Submission date: June 2012
Supervisor: Svein Sunde, IMTE
Co-supervisor: Morten Tjelta, IMT

Norwegian University of Science and Technology
Department of Materials Science and Engineering

ABSTRACT

The possibilities for using $CaNb_2O_6$ as a photocatalyst in direct water splitting have been evaluated by investigating the electronic structure of the material. In addition the oxide was doped with nitrogen in order to modify the electronic structure and obtain visible light absorption. Experimental techniques such as electrochemical impedance spectroscopy (EIS), photocurrent, and diffuse reflectance spectroscopy (DRS) were combined with theoretical approaches to determine the bandgap, flatband potential and quasi-Fermi levels of the photocatalyst.

$CaNb_2O_6$ was prepared by a sol-gel synthesis and doped with nitrogen by heat treatment of the oxide powder in an ammonia atmosphere. X-ray diffraction (XRD) confirmed phase pure orthorhombic $CaNb_2O_6$ for both pure and N-doped oxide and excluded a possible transformation of the oxide into an oxynitride. Upon illumination anodic photocurrents were observed implying that $CaNb_2O_6$ was an n-type semiconductor due to oxygen vacancies in the lattice. From the wavelength dependency of the photocurrent a direct bandgap of 3.7eV and an indirect bandgap of 3.4eV were determined for undoped $CaNb_2O_6$. Doping with nitrogen altered the optical properties of the oxide and shifted the absorption edge into the visible light region. Calculations using the density functional theory (DFT) attributed the change in absorption properties to the formation of narrow energy bands above the valence band of pure $CaNb_2O_6$. An alternative explanation could be a hybridization of N 2p and O 2p bands. Correspondingly a reduction of the bandgaps for N-doped $CaNb_2O_6$ with respect to the undoped oxide was identified.

Impedance was applied to determine the flatband potential of $CaNb_2O_6$ from Mott-Schottky plots. However the obtained results seemed to be dominated by contributions from the electrode substrate. Theoretical investigations concluded that pinhole-free oxide layers creating an ohmic contact with the substrate are required in order to designate the observed impedance response to the space charge capacitance.

Quasi-Fermi level measurements indicated a low photocatalytic activity of $CaNb_2O_6$ as no photocurrent could be detected. Further investigations are needed to identify the cause of the photocurrent limitations. Nevertheless probable explanations could be low conductivity in $CaNb_2O_6$, high concentrations of recombination centers or slow charge transfer kinetics. The latter was confirmed for porous oxide layers as the addition of a hole scavenger increased the measured photocurrent. Positive photocurrent transients were also observed for porous $CaNb_2O_6$ films and could be related to either the diffusion of electrons through the porous oxide layer or to a photoanodic decomposition of the photocatalyst.

SAMMENDRAG

Mulighetene for å bruke $CaNb_2O_6$ som fotokatalysator i direkte vannsplitting ble undersøkt ved å bestemme elektronstrukturen til materialet. Oksidet ble i tillegg dopet med nitrogen for å endre elektronstrukturen og oppnå absorpsjon av synlig lys. Eksperimentelle teknikker som elektrokjemisk impedans spektroskopi, fotostrøm og diffus reflektans spektroskopi ble kombinert med teoretiske tilnærminger for å finne båndgap, flatbåndpotensial og kvasi-Fermi nivåer til fotokatalysatoren.

$CaNb_2O_6$ ble produsert ved å anvende en sol-gel syntese og deretter dopet med nitrogen ved å varmebehandle oksidpulveret i en ammoniakkatmosfære. Røntgendiffraksjon bekreftet en ren fase av ortorombisk $CaNb_2O_6$ for både rent og nitrogen dopet oksid noe som utelukket en omdanning av oksidet til et oksynitrid. Ved belysning ble anodiske fotostrømmer observert og antydet at fotokatalysatoren er en n-type halvleder på grunn av oksygenvakanser i gitteret. Fra fotostrømmens endring med lysets bølgelengde ble et direkte båndgap på 3.7eV og et indirekte båndgap på 3.4eV bestemt for udopet $CaNb_2O_6$. Nitrogendoping endret de optiske egenskapene til oksidet og forskjøv absorpsjonskanten inn i synlig lys-området. DFT beregninger tilskrev endringen i absorpsjonegenskaper til dannelsen av smale energibånd over valensbåndet til rent $CaNb_2O_6$. En alternativ forklaring basert på hybridisering av N 2p og O 2p bånd ble også foreslått, og en reduksjon i båndgapet for nitrogendopet $CaNb_2O_6$ i forhold til udopet oksid ble funnet.

Impedans ble anvendt for å bestemme flatbåndpotensialet til $CaNb_2O_6$ ved bruk av Mott-Schottky plott. Imidlertid så resultatene ut til å være dominert av bidrag fra elektrodesubstratet. En teoretisk studie konkluderte med at et hullfritt oksidsjikt med en ohmsk kontakt mot substratet var nødvendig for å kunne måle romladningskapasitansen i impedansmålinger.

Kvasi-Fermi nivå målinger indikerte at $CaNb_2O_6$ hadde lav fotokatalytisk aktivitet siden ingen fotostrøm ble detektert. Videre undersøkelser er nødvendig for å identifisere årsaken til begrensningene i fotostrøm. Likevel vil sannsynlige forklaringer inkludere lav ledningsevne i $CaNb_2O_6$, høye konsentrasjoner av rekombinasjonssentre eller en langsom ladningsoverføringskinetikk. Sistnevnte ble bekreftet for porøse oksid lag ved å måle en økt fotostrøm ved tilsats av en hullsoper til elektrolytten. Positive fotostrømtransienter ble også observert for porøse $CaNb_2O_6$ filmer og ble forklart med enten diffusjon av elektroner gjennom det porøse oksidlaget, eller av en fotoanodisk nedbryting av fotokatalysatoren.

PREFACE

This Master thesis has been carried out at the Department of Materials Science and Engineering at the Norwegian University of Science and Technology (NTNU) during spring 2012 as part of a Master of Science degree in Materials Chemistry and Energy Technology. The thesis is a continuation of a project work performed at the same department in the fall 2011. A PhD project is closely related to this Master thesis and most of the work has been done in close collaboration with PhD candidate Morten Tjelta.

The main goal of this Master thesis was to evaluate the possibilities for using the semiconducting material $CaNb_2O_6$ as a photocatalyst in water splitting. This was done by characterizing the electronic structure and optical properties of both pure and nitrogen doped $CaNb_2O_6$ photoanodes in aqueous solutions. Applied experimental techniques included impedance, photocurrent and diffuse reflectance measurements. The obtained results along with a consideration of the material's possible application in water splitting are presented in this report.

All the work associated with this Master thesis has been carried out independently, honest, and in accordance with the examination regulations at NTNU.

I would like to express gratitude to my supervisor, Professor Svein Sunde, for weekly meetings consisting of careful explanations and discussions regarding my thesis. A heap of thanks goes to PhD candidate Morten Tjelta for always being available to answer my questions, share his knowledge, and help me with the experimental work. I would also like to thank May Grete Sætran and all the PhD candidates and master students in the Electrochemical Energy group for training, discussions, and help when needed. Finally I thank the lovely chemistry girls and my crazy family in Abels gate for always listening to my problems and keeping my spirits up. I'll miss y'all so much!

Trondheim, June 2012

Marthe Emelie Melandsø Buan

CONTENTS

List of abbreviations

CB	Conduction band
CE	Counter electrode
DFT	Density functional theory
DOS	Density of states
DRS	Diffuse reflectance spectroscopy
EIS	Electrochemical Impedance Spectroscopy
GC	Glassy carbon
HOPG	Highly ordered pyrolytic graphite
ITO	Indium tin oxide
JDOS	Joint density of states
KM	Kubelka Munk
N500	N-doped $CaNb_2O_6$ at 500°C
N600	N-doped $CaNb_2O_6$ at 600°C
N700	N-doped $CaNb_2O_6$ at 700°C
PEC	Photoelectrochemical
PZC	Point of zero charge
RDE	Rotating disk electrode
RE	Reference electrode
RHE	Reversible hydrogen electrode
SHE	Standard hydrogen electrode
VB	Valence band
WE	Working electrode
XRD	X-ray diffraction

1 Introduction

Due to an increasing energy consumption the reserves of fossil fuels will not be sufficient to cover the future energy needs [1]. In addition the combustion of fossil fuels produces greenhouse gasses associated with the global climate change. An essential way of facing the future energy needs is the development of efficient ways to exploit clean renewable energy sources. Today solar energy combined with the use of hydrogen as energy carrier is one of the most promising future energy sources [2].

The most straight forward method to produce hydrogen from water and sunlight is by combining solar cells and water electrolysis. However the overall conversion efficiency is still quite limited [3]. A potentially more attractive alternative is solar hydrogen production from direct photoelectrochemical (PEC) water splitting. The photocatalytic splitting of water into H_2 and O_2, reaction (1.1), was first described by Fujishima and Honda [4] by irradiating a TiO_2 photoanode while applying an external bias.

$$2H_2O + h\nu \rightarrow 2H_2 + O_2 \tag{1.1}$$

Since the discovery of PEC water splitting the potential applications for solar energy conversion and storage has been widely studied. This has resulted in the development of a range of PEC cells and research on several different photocatalytic materials [5-7]. The main goal of the research is to achieve highest possible efficiency by obtaining high catalytic activity and efficient charge transfer. Nevertheless, due to a lack of photocatalytic materials with appropriate electronic structure and stability most of the systems proposed so far have yielded low quantum efficiencies or been rather complicated [3].

Typical photocatalyst materials investigated have been various semiconducting metal oxides possessing large bandgap energies of 3-4eV [7, 8]. Thus a narrowing of the bandgap is required in order to obtain visible light absorption (1.5 - 3.1eV). Additionally the positions of the energy band edges need to allow for the reduction and oxidation of water. In an attempt to fulfill these requirements band engineering can be employed, i.e. modifying the band structure of the material by doping, valence band formation or synthesis of solid solutions [9, 10].

In order to develop efficient photocatalyst materials for water splitting knowledge of the material's electronic structure and how it depends on changes in the electrochemical system is important. Several photoelectrochemical and electrochemical methods have been developed in order to characterize properties such as bandgap, Fermi levels and flatband potential of semiconducting materials. These methods include optical- and PEC measurements, different microscope techniques and electrochemical impedance spectroscopy (EIS) [11-14].

The principal objective of this Master thesis is to combine different experimental techniques with theoretical approaches in order to determine the electronic structure of both pure and nitrogen doped calcium niobate, $CaNb_2O_6$. This material is currently being considered as a catalyst for photocatalytic splitting of water and knowledge of its band structure and behavior in aqueous electrolytes is an essential part of the evaluation. Altering of the electronic structure of $CaNb_2O_6$ by doping with nitrogen will be an important part of this thesis. The main goal with the doping is to enhance the efficiency of the photocatalyst by obtaining visible light absorption. Nitrogen doping will be done by exposing the oxide to an ammonia atmosphere at elevated temperatures as described by among others Cho et al. [15].

2 Theory

In order to understand the concepts behind photoelectrochemical devices knowledge on the interaction between semiconductors and electrolytes is indispensable. This chapter aims to introduce the most important properties of semiconductors and electrolytes and explain in brief what could happen when a semiconductor is immersed in an electrolyte and irradiated. Also the general aspects and theory behind different techniques used to characterize semiconductor properties will be discussed.

2.1 Semiconductor electrochemistry

2.1.1 Energy levels in semiconductors

The properties of semiconductors can to a large extent be described by their electronic band structure which can be obtained by solving the Schrödinger equation [12]. The solution shows that all semiconductors possess a forbidden energy region termed the bandgap, E_g, in which energy states cannot exist. This region lies between the lowest unoccupied energy band called the conduction band (CB) and the highest occupied energy band called the valence band (VB).

If both the lowest minimum of the conduction band, E_c, and the highest maximum of the valence band, E_v, occur at the same wave vector k, the corresponding energy gap is termed a direct bandgap as illustrated to the left in Figure 2.1. If on contrary the conduction band minimum is found at a different k-vector the energy gap is termed an indirect bandgap. A transition from the VB to the CB will then require a change in crystal momentum by a phonon ($h\omega$) [16].

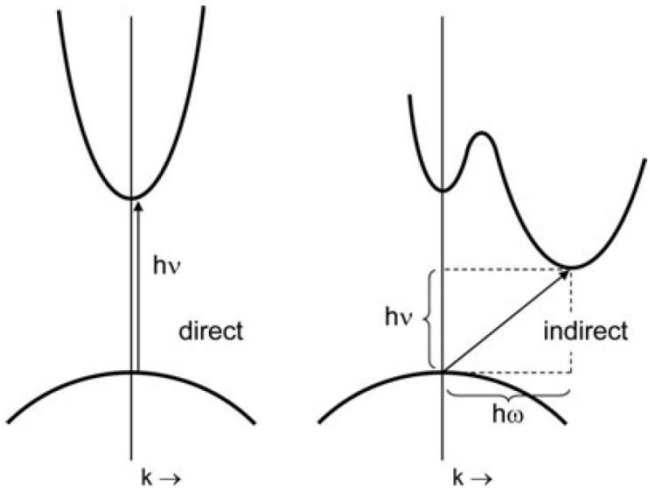

Figure 2.1 : Direct (left) and indirect (right) bandgap of a semiconductor [16].

The Fermi energy, E_F, of a semiconductor is defined as the energy of the topmost filled orbital at absolute zero [11]. At temperatures above absolute zero the distribution of electrons in the semiconductor is describes by Fermi-Dirac statistics. The probability that an energy level E is occupied by an electron at an absolute temperature T is then given by the Fermi function $f(E)$ where k is the Boltzmann constant [17]:

$$f(E) = \frac{1}{1 + \exp\left(\frac{E - E_F}{kT}\right)} \tag{2.1}$$

At energy levels slightly below E_F the occupation probability becomes unity while at energy levels a few kT above E_F it tends towards zero. Thus the probability of occupancy is ½ at the Fermi level for an absolute temperature T.

For an intrinsic (i.e. undoped) semiconductor the Fermi energy will be situated close to the middle of the bandgap as shown in Figure 2.2 (a). This is because the last term in equation (2.2) will be small when the effective masses of holes and electrons are almost equal $m_h^* \approx m_e^*$ [18].

$$E_F = \frac{1}{2}E_g + \frac{3}{4}kT \ln\left(\frac{m_h^*}{m_e^*}\right) \approx \frac{1}{2}E_g \tag{2.2}$$

For an extrinsic (i.e. doped) semiconductor energy levels are introduced within the bandgap. A semiconductor doped with electron donors is called n-type and has a Fermi level just below the conduction band edge, Figure 2.2 (b). Doping with electron acceptors yields a p-type semiconductor with a Fermi level just above the valence band edge as illustrated in Figure 2.2 (c).

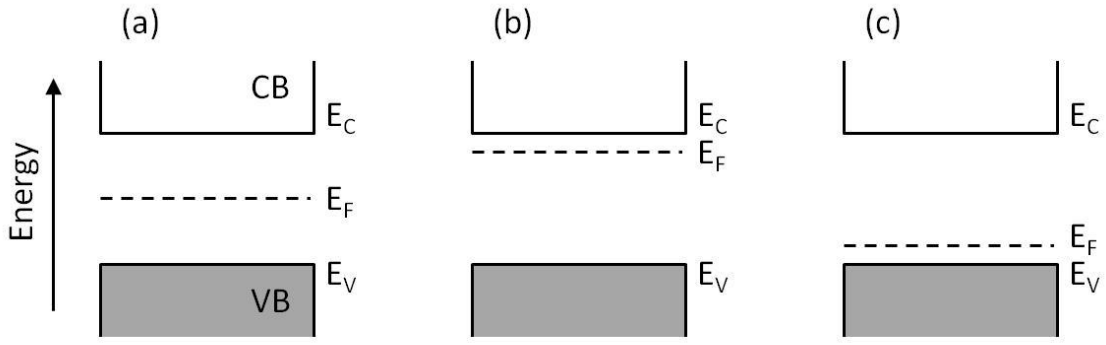

Figure 2.2 : Energy levels for (a) an intrinsic semiconductor, (b) an n-type semiconductor and (c) a p-type semiconductor.

At equilibrium the Fermi level is constant throughout the semiconductor and equal for both holes and electrons. This equilibrium will be altered when the semiconductor is irradiated by light with energy larger than the bandgap since electron-hole pairs are created within the semiconductor. The densities of electrons and holes in the semiconductor will then change and can no longer be described by the same Fermi level. Accordingly, the quasi-Fermi levels $E_{F,n}$ and $E_{F,p}$ of electrons and holes respectively are introduced [12]:

$$E_{F,n}(x) = E_C - kT \ln\left(\frac{N_C}{n(x)}\right) \tag{2.3}$$

$$E_{F,p}(x) = E_V + kT \ln\left(\frac{N_V}{p(x)}\right) \tag{2.4}$$

In the above equations $n(x)$ and $p(x)$ denote the concentration of electrons and holes at a position x in the semiconductor while N_C and N_V are the density of states near the conduction band edge and valence band edge respectively. For an n-type semiconductor $E_{F,n}$ will remain unchanged with respect to the equilibrium case whereas $E_{F,p}$ is shifted downwards during irradiation. This is due to the high initial concentration of electrons, n_0, and low initial concentration of holes, p_0, in an n-type semiconductor as explained by equation (2.5) and (2.6).

$$n(x) = n_0 + \Delta n(x) \approx n_0 \tag{2.5}$$

$$p(x) = p_0 + \Delta p(x) \approx \Delta p(x) \tag{2.6}$$

Since the light penetration often is small the excitation of electron-hole pairs occurs at the surface of the semiconductor. Some of the charge carriers will then diffuse out of the excitation range and recombine. In consequence the quasi-Fermi level of holes for an n-type semiconductor varies with the distance from the excitation area as illustrated in Figure 2.3 (c) [12].

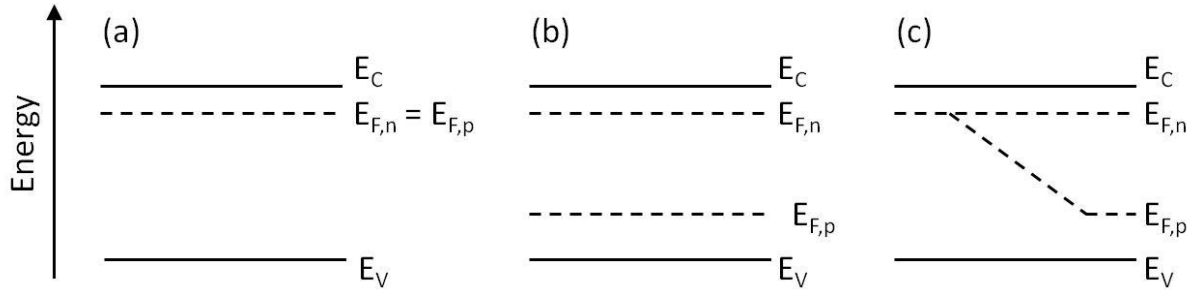

Figure 2.3 : Quasi-Fermi levels of electrons and holes (a) at equilibrium, (b) under irradiation and (c) for local excitation.

2.1.2 Energy levels in electrolytes

The electrochemical potential, $\bar{\mu}_{e,redox}$, of an electron in a simple electrolyte is given by equation (2.7), where c_{ox} and c_{red} are the concentrations of the oxidized and reduced species of the redox couple and μ^0_{redox} is the standard chemical potential for c_{ox}=c_{red} [19]:

$$\bar{\mu}_{e,redox} = \mu^0_{redox} + kT \ln\left(\frac{c_{ox}}{c_{red}}\right) \tag{2.7}$$

The Fermi level of the electrolyte, $E_{F,redox}$, corresponds to the electrochemical potential when the redox system is related to the vacuum level reference, i.e. the energy scale where the energy of a free electron in vacuum is taken as zero. Since electrochemical potentials normally are related to the standard hydrogen electrode (SHE), the energy of the H_2/H^+ couple with respect to the vacuum level has been estimated both theoretical and experimental. Different approaches yield different values and the value usually employed is -4.5eV calculated by Lohmann [12]. Accordingly the relation between the Fermi level and the redox potential E^0_{redox} of the electrolyte vs. SHE can be described by equation (2.8) where e is the charge of an electron:

$$E_{F,redox} = -4.5eV - eE^0_{redox} \tag{2.8}$$

In order to describe charge transfer between electrodes and redox couples Gerischer [20] developed a model based on electronic energy levels. In this model the energy levels of an electrolyte are given by the work functions of the components in the redox couple. Reduced species represent occupied electron energy states while oxidized species correspond to unoccupied states. Thus the electronic energy E^0_{red} in Figure 2.4 (a) represents the energy required to transfer an electron from the reduced species into vacuum leading to the formation of the oxidized species. This energy corresponds to the ionization energy. For the reverse process where an electron in vacuum is captured by the oxidized state to form the reduced species the energy required is E^0_{ox} which corresponds to the electron affinity.

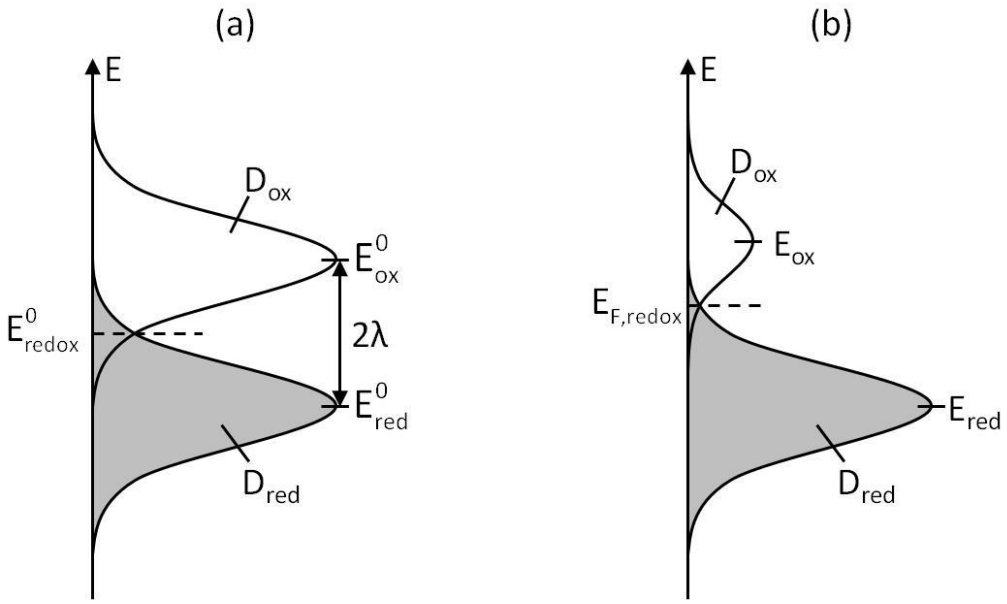

Figure 2.4 : Energy levels of a redox electrolyte for (a) $c_{ox} = c_{red}$ and (b) $c_{ox} << c_{red}$. λ represents the reorganization energy.

In polar solvents such as water the ions in the electrolyte are surrounded by oriented solvent molecules. Due to the thermal motions of the solution the energy level of the central ion will fluctuate and lead to a broadening of the electronic levels of the redox system. If any variation in the solvation shell can be described by harmonic oscillations, the distributions of electronic levels of the redox system is given by [12]:

$$W_{ox}(E) = \frac{1}{\sqrt{4\pi\lambda kT}} \exp\left[-\frac{(E - E^0_{redox} + \lambda)^2}{4kT\lambda} \right] \tag{2.9}$$

$$W_{red}(E) = \frac{1}{\sqrt{4\pi\lambda kT}} \exp\left[-\frac{(E - E^0_{redox} - \lambda)^2}{4kT\lambda} \right] \tag{2.10}$$

The distribution functions $W_{ox}(E)$ and $W_{red}(E)$ describe the probabilities of finding the empty and occupied electronic state, respectively, at an energy E. The parameter λ is called the reorganization energy and represents the electrostatic energy required to reorganize the solvent dipoles surrounding an ion after the ion has been reduced or oxidized. The Franck-Condon principle is assumed to be valid, i.e. the electron transfer is very fast compared to the reorganization of the solvation shell and solvent dipoles. According to equation (2.11) the density of states (DOS) is proportional to the concentrations of the electrolyte species:

$$D_{ox}(E) = c_{ox} W_{ox}(E); \qquad D_{red}(E) = c_{red} W_{red}(E) \tag{2.11}$$

The corresponding distributions are illustrated in Figure 2.4 for both equal and different concentrations of the reduced and oxidized species. By varying the concentration of one of the species the Fermi level of the redox system is shifted according to the Nernst equation [21], equation (2.12). For dilute solutions the activity coefficients are close to unity and concentrations can be used instead of activities. In the Nernst equation R represents the gas constant, n the number of electrons transferred in the redox reaction and F the Faraday constant:

$$E_{F,redox} = E^0_{redox} - \frac{RT}{nF} \ln\left(\frac{c_{ox}}{c_{red}}\right) \tag{2.12}$$

2.1.3 Semiconductor-electrolyte junction

When a semiconductor is immersed in an electrolyte, the system will be in equilibrium when the electrolyte and the semiconductor possess the same Fermi level [19]:

$$E_F = E_{F,redox} \tag{2.13}$$

This means that charge will be transferred across the semiconductor-electrolyte interface until equilibrium is established. If the Fermi level of the electrolyte is situated in the middle of the bandgap of an n-type semiconductor electrons will be transferred from the semiconductor to the electrolyte, see Figure 2.5 (a).

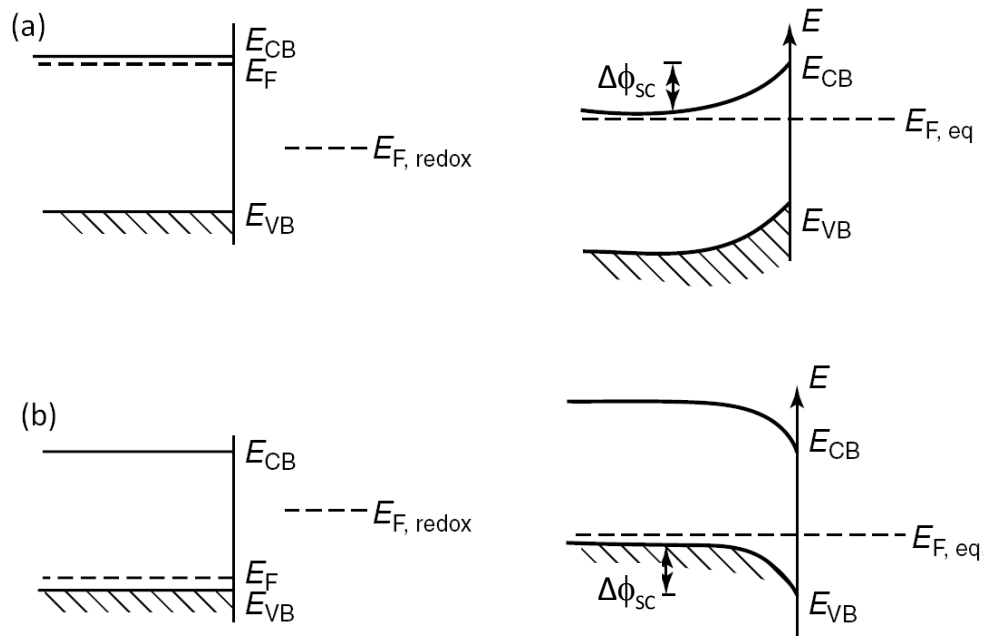

Figure 2.5 : Energy levels in the semiconductor and redox electrolyte before (left) and after (right) equilibration for (a) an n-type semiconductor and (b) a p-type semiconductor [11]. $\Delta\Phi_{SC}$ represents the potential drop across the space charge region in the semiconductor.

Since the carrier density is small in semiconductors, the charge transfer will create a region with ionized donors a certain range below the semiconductor surface. The positive space charge in an n-type semiconductor induces an electric field and as a consequence the bands of the semiconductor will be bent downwards from the surface. Vice versa for a p-type semiconductor, Figure 2.5 (b), where electrons from the electrolyte will flow into the semiconductor creating a negative space charge and bending the bands upwards. The corresponding potential drop across the space charge region is termed $\Delta\Phi_{SC}$.

The potential and charge distribution within the space charge region is quantitatively described by Poisson's equation [18], where $\rho(x)$ is the charge density at a distance x from the surface, ε the dielectric constant and ε_0 the permittivity of vacuum:

$$\frac{d^2\Delta\phi_{SC}}{dx^2} = -\frac{\rho(x)}{\varepsilon\varepsilon_0} \tag{2.14}$$

By solving the Poisson equation a differential capacitance of the space charge region can be deduced [12], as will be discussed in more detail in section 2.4.5.

For a semiconductor in an aqueous solution, protons and hydroxide ions will continuously adsorb and desorb from the surface creating a dynamic equilibrium. The specific adsorption of these ions at the surface depends on the pH of the solution. The pH at which the net adsorbed charge is zero is called the point of zero charge (PZC) of the semiconductor. Specifically adsorbed ions will, along with oriented solvent dipoles, create a potential drop in the solution close to the surface termed the Helmholtz potential, $\Delta\Phi_H$ [16]:

$$\Delta\phi_H = \frac{2.3kT}{e}(PZC - pH) \tag{2.15}$$

The region holding the potential drop is termed the Helmholtz layer and has a width of approximately 2-5Å. The Helmholtz potential will change with -59mV (2.3kT/e) per pH unit at 25°C according to equation (2.15) because of protonation and deprotonation of surface hydroxyl groups. Subsequently the position of the band edges of the semiconductor at the electrochemical scale will ideally be shifted cathodically with 59mV per increase in pH unit.

The total potential drop across the semiconductor-electrolyte interface, $\Delta\Phi_{tot}$, will therefore not only occur in the space charge region of the semiconductor, $\Delta\Phi_{SC}$, but also in the Helmholtz layer of the electrolyte, $\Delta\Phi_H$. In dilute solutions a diffuse double layer in the electrolyte called the Gouy layer will also be present, but this can be neglected for electrolytes with high ion concentrations. The total potential difference across the interface measured vs. a reference electrode is then given by [12]:

$$\Delta\phi_{tot} = \Delta\phi_{SC} + \Delta\phi_H \tag{2.16}$$

At the open circuit potential the system is in a dynamic equilibrium meaning that the anodic and cathodic currents across the interface are equal and no net current is measured. By applying an external bias to the system the size of the space charge region will be altered when assuming that the Helmholtz layer is not affected by the potential change. This is termed band edge pinning since the edges of the energy bands at the surface will remain fixed during the potential change. When considering an n-type semiconductor a forward bias will induce a cathodic current and increase the amount of electrons in the space charge region. As a consequence the energy bands of the semiconductor are bent upwards as shown in Figure 2.6 (c). Similarly an anodic current will result from applying a reverse bias to the system and the bands of the n-type semiconductor will be bent downwards as the size of the space charge region increases, Figure 2.6 (b).

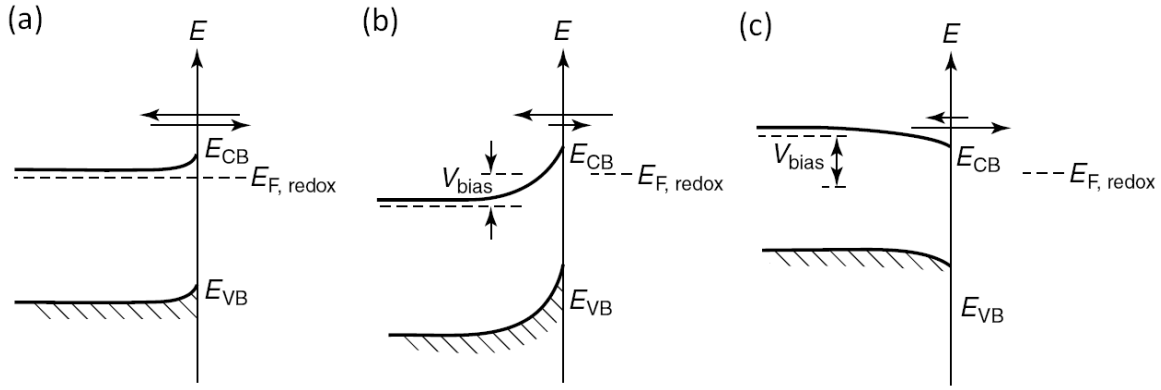

Figure 2.6 : An n-type semiconductor-electrolyte interface (a) at equilibrium, (b) under reverse bias and (c) under forward bias [11].

For a certain external bias applied to the semiconductor the width of the space charge region will approach zero and there will not be any potential drop in the semiconductor. The energy bands of the semiconductor will then be flat. The applied potential required to give flat energy bands is termed the flatband potential, V_{fb}. This potential can among others be determined experimentally using the Mott-Schottky relation [19], see section 2.4.5, by photocurrent onset potential measurements [14, 22], from the Gärtner relation [23], see section 2.4.1, or by measuring the quasi-Fermi level of semiconductor particles in suspensions [24], see section 2.4.2. From the flatband potential the energies of both the conduction and valence band at the surface (the band edges) can be determined if the size of the bandgap is known.

If however the potential drop across the Helmholtz layer changes when applying an external potential to the system the band edges are no longer pinned. This could happen due to Fermi level pinning by surface states, trapping of photogenerated minority carriers in surface states [25] or by a low rate of minority carrier transfer across the semiconductor-electrolyte interface [19]. Unpinning of the band edges by surface states will be further discussed in the following section.

2.1.4 Surface states

Surface states at the semiconductor-electrolyte interface generally arise from the termination of the periodic crystal lattice at the surface of the semiconductor [12]. The chemical nature of surface states depends strongly on the bonding character of the material. For covalent materials “dangling bonds” can act as electron donors or acceptors creating Shockley surface states mainly located near the middle of the bandgap. Metal oxides are however often highly polar or even ionic due the high electronegativity of oxygen. In such ionic materials Tamm states can be formed by coordinatively unsaturated ions at the surface. Lattice oxygen at the surface can form deep donor states just above the VB while lattice metal ions can form deep acceptor states just below the conduction band [16]. The electronic structure at the surface will therefore often be different compared to that in the bulk. This can affect the charge transfer reactions in the electrochemical system since the localized surface states might exchange charge with both the energy bands and the redox electrolyte.

The presence of surface states can lead to pinning of the Fermi level at the energies of the surface states rather than band edge pinning. A change in the system by changing e.g. the redox electrolyte or the applied potential will then lead to a shift of the energy bands instead of the Fermi level. This can be explained by trapping of minority carriers in the surface states. An accumulation of minority carriers at the surface will result in a smaller space charge inside the semiconductor. Subsequently at high enough densities of surface states all of the potential change will take place in the Helmholtz layer rather than in the space charge layer. It is important to note that the Fermi level pinning might also have other origins such as band inversion or accumulation, corrosion reactions and limitations imposed by bulk recombination processes [18]. Figure 2.7 illustrates a semiconductor-electrolyte junction with surface states present in the bandgap. The rates at which the surface states can trap electrons, k_n, and holes, k_p, are shown in addition to the rate of bulk recombination k_b.

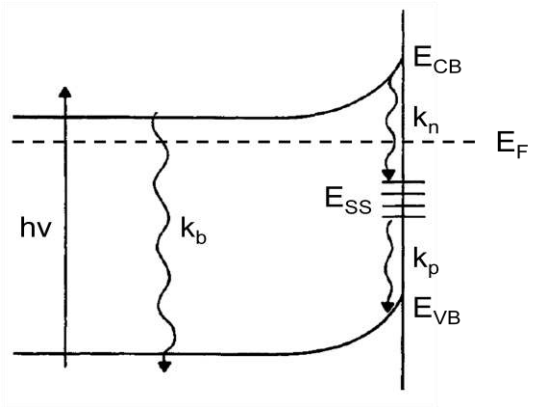

Figure 2.7 : Excitation and recombination processes of electrons and holes in an n-type semiconductor with surface states present in the bandgap [18].

The occupation of the surface states by electrons depends on the position of the Fermi level with respect to the surface states. The charge stored in the surface states Q_{ss} is given by [12]:

$$Q_{ss} = efN_{ss} \tag{2.17}$$

Here e is the charge of an electron, N_{ss} the density of surface states and f the Fermi-Dirac distribution as defined in section 2.1.1:

$$f(E_{ss}) = \frac{1}{1+\exp\left(\frac{E_{ss}-E_F}{kT}\right)} \tag{2.18}$$

Since the distance between the Fermi level E_F and the energy bands depends on the potential drop across the space charge region $\Delta\Phi_{SC}$, the charge Q_{ss} will also vary with the potential drop. The differential surface state capacitance C_{ss} can thus be defined as:

$$C_{ss} = \frac{dQ_{ss}}{d\Delta\phi_{SC}} = eN_{ss}\frac{df}{d\Delta\phi_{SC}} \tag{2.19}$$

The dependency of the surface state capacitance, C_{ss}, and the Fermi distribution, f, with the potential change across the space charge region is graphically represented in Figure 2.8.

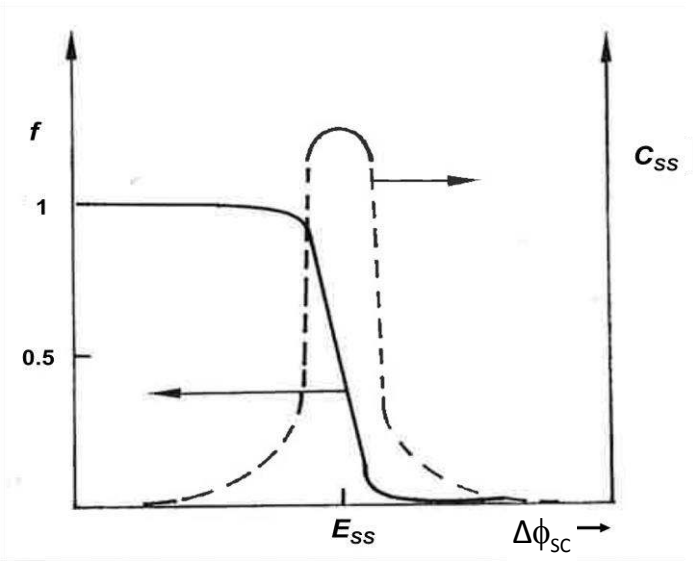

Figure 2.8 : The Fermi distribution f and surface state capacity C_{ss} as functions of the potential across the space charge layer $\Delta\Phi_{SC}$ [12].

2.1.5 Charge transfer

Charge transfer processes between the semiconductor and the electrolyte can only occur via the conduction or valence band of the semiconductor [12]. The transfer takes place via tunneling and is thus an iso-energetic process. This implies that the electron transfer is much faster than any reorganization of the solvation shell or the solvent dipoles (Frank-Condon principle). The rate of the charge transfer is proportional to the surface concentration of free electrons and holes, n_s and p_s, in the conduction and valence band respectively. The densities are related to the bulk charge carrier densities, n_0 and p_0, as shown by equation (2.20).

$$n_s = n_0 \exp\left(-\frac{e\Delta\phi_{SC}}{kT}\right); \qquad p_s = p_0 \exp\left(\frac{e\Delta\phi_{SC}}{kT}\right) \tag{2.20}$$

In addition the rate of charge transfer is proportional to the density of states (DOS) of the electrolyte given by equation (2.11). A large overlap between the redox DOS with the energy of the charge carrier will give higher currents than a small overlap as illustrated in Figure 2.9.

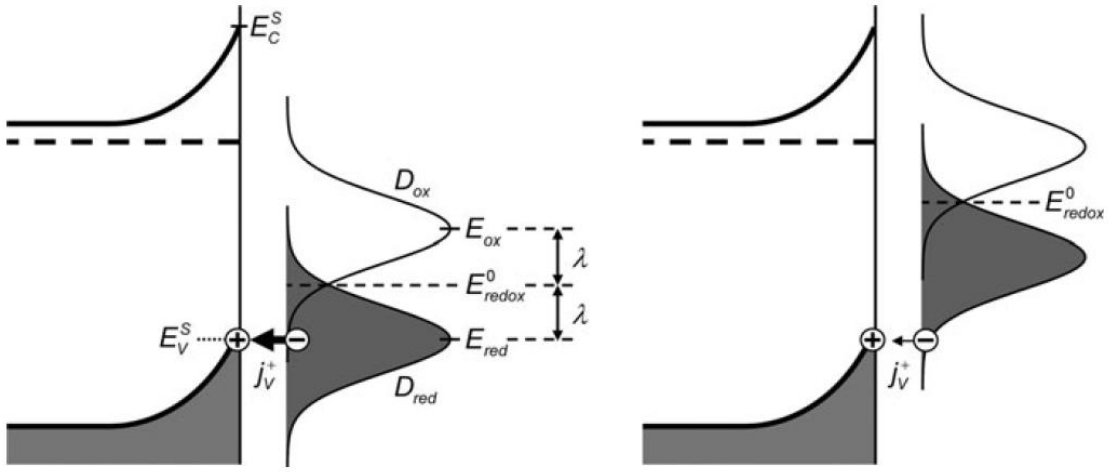

Figure 2.9 : Electron transfer from the redox electrolyte to the semiconductor valence band. A large overlap (left) gives a higher current than a small overlap (right) [16].

The anodic (+) and cathodic (-) valence and conduction band currents can be written as [16]:

$$j_V^+ = ek_V^+ p_s D_{red}(E_V^s); \qquad j_V^- = ek_V^- N_V D_{ox}(E_V^s) \tag{2.21}$$

$$j_C^+ = ek_C^+ N_C D_{red}(E_C^s); \qquad j_C^- = ek_C^- n_s D_{ox}(E_C^s) \tag{2.22}$$

Here N_V and N_C are the DOS at the upper edge of the valence band (at $E=E_v^s$) and lower edge of the conduction band (at $E=E_c^s$) and k different rate constants. Since j_c^+ and j_v^- only contain constant parameters they are independent of the electrode potential while j_c^- and j_v^+ depends on the potential via n_s and p_s.

Under illumination minority carriers will be generated in the space charge region of the semiconductor and driven towards the interface by the electric field. Minority carriers produced in the bulk can diffuse to the space charge region and enhance the interfacial current. The amount of carriers diffusing into the space charge region depends on the lifetime of the minority carriers, i.e. how long it takes before they recombine. Reichman's method [12] can be applied to derive an expression for the photocurrent density under illumination. When considering an n-type semiconductor the hole density can be obtained by solving the diffusion equation for minority carriers produced in the bulk:

$$D\frac{d^2p}{dx^2} - \frac{p - p_0}{\tau} + I_0\alpha\exp(-\alpha x) = 0 \tag{2.23}$$

The first term describes the diffusion, the second the recombination and the third the generation of holes in the semiconductor. In equation (2.23) D is the diffusion coefficient, τ the lifetime of the holes, α the absorption coefficient of the semiconductor, p_0 the equilibrium hole density, I_0 the monochromatic photon flux and x the distance from the surface. By applying the boundary conditions that $p=p_0$ at $x=\infty$ and $p=p_d$ at $x=d_{SC}$ the following expression for the total valence band photocurrent in an n-type semiconductor is obtained.

$$j_V = \frac{j_g - j_0\exp\left(\frac{-e\eta}{kT}\right)}{1 + \frac{j_0}{j_V^0}\exp\left(\frac{-e\eta}{kT}\right)} \tag{2.24}$$

Here j_g is the generation current, j_V^0 the hole transfer rate at the interface and j_0 the saturation current density, i.e. the hole current in the valence band when x equals the width of the space charge region and $I_0=0$.

2.1.6 Semiconductor particles

In principle the same charge transfer processes should occur at semiconductor particles and bulk electrodes. However, an oxidation and a reduction must always occur simultaneously at a semiconductor particle, otherwise the particle would become charged [12]. For nanoparticles there will not be enough room or charges for the presence of a space charge region and hence the bands will be flat as illustrated in Figure 2.10 b). In larger particles a space charge layer can be present, but electron transfer from the CB will still occur upon light excitation. The transfer of holes to an electron donor D will lead to a negative charging of the particle causing a reduction of the space charge region and hence a flattening of the energy bands will occur as shown in Figure 2.10 a).

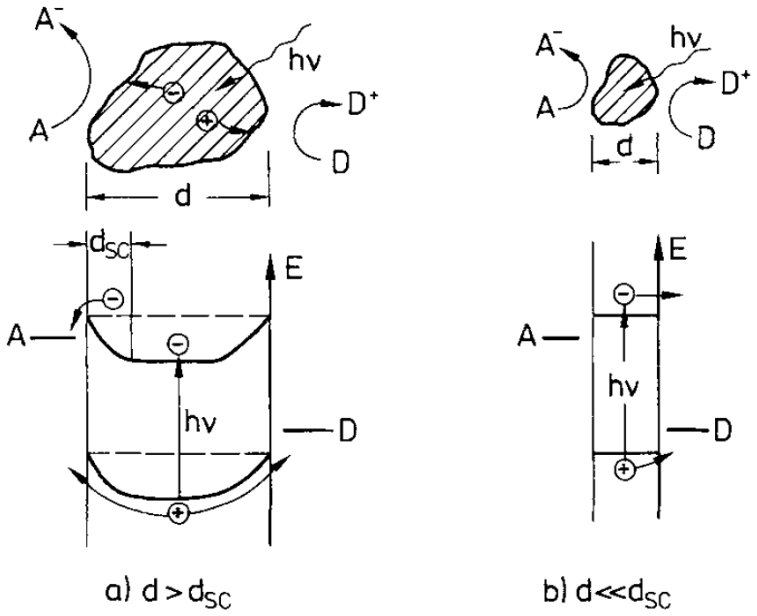

Figure 2.10 : Electron and hole transfer at large (a) and small (b) semiconductor particles to an electron acceptor A and an electron donor D [12].

Suspensions of semiconductor particles can be used to investigate the charge transfer of irreversible reactions at the surface when both a hole acceptor and an electron acceptor is present in the electrolyte. In addition the quasi-Fermi level of electrons in the semiconductor particles can be determined by polarizing a metallic collector electrode so that it accepts electrons from the suspension [14]. This method will be further discussed in section 2.4.2.

2.2 Water splitting

An energy diagram of a PEC cell for water splitting based on an n-type semiconductor as photoanode and a metal as cathode is shown in Figure 2.11. In the setup an anodic bias is applied in order to increase the potential drop across the space charge region and ensure an effective separation of the electron-hole pairs.

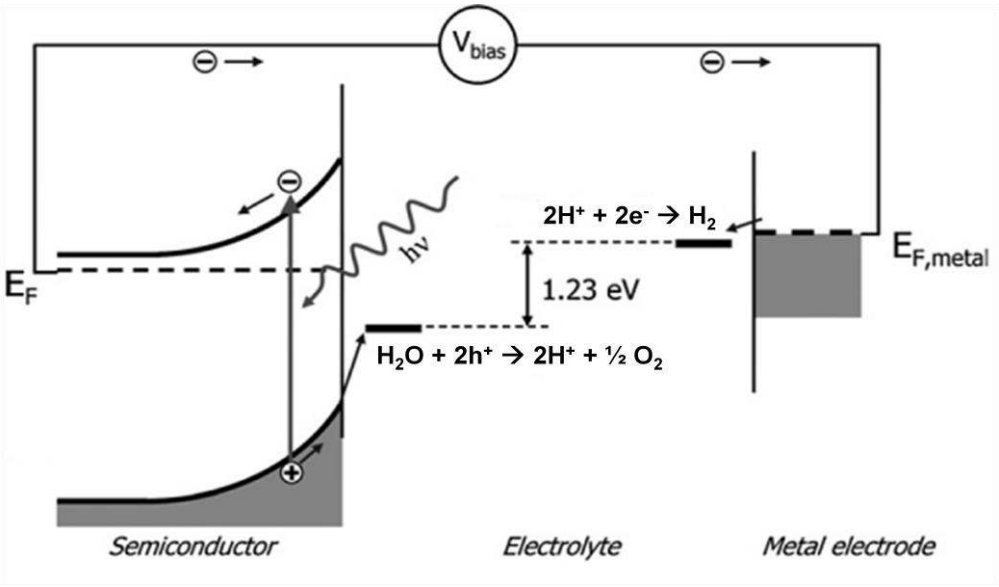

Figure 2.11 : Energy diagram of a PEC cell for direct water splitting using an n-type semiconductor under anodic bias as photoanode [3].

When the semiconductor is irradiated by light with energy larger than the bandgap electrons can be excited from the valence band into the conduction band and electron-hole pairs are created. Because of the potential drop in the space charge region the excited electrons will be swept into the bulk of the semiconductor while the holes will be driven towards the semiconductor-electrolyte interface. If the holes reach the interface before recombining they can react with the electrolyte and oxidize water, reaction (2.25). Similarly if the electrons diffuse through the bulk of the semiconductor without recombining they will reach the metal electrode where they can reduce protons and produce hydrogen gas, reaction (2.26). The total redox-reaction corresponds to the splitting of water into hydrogen and oxygen gas as shown in reaction (2.27):

$$\text{Anode: } H_2O + 2h^+ = 2H^+ + \frac{1}{2}O_2 \tag{2.25}$$

$$\text{Cathode: } 2H^+ + 2e^- = H_2 \tag{2.26}$$

$$\text{Total: } H_2O = H_2 + \frac{1}{2}O_2 \tag{2.27}$$

In order to achieve water splitting in the PEC cell it is essential that the valence band edge of the semiconductor lies below the potential for oxidation of water, $E(O_2/H_2O)$. Otherwise the holes will not be able to oxidize water as they do not possess sufficient energy. The same applies for the counter electrode that needs to possess a Fermi level superior to the potential for reduction of protons, $E(H^+/H_2)$. Since the Fermi level of the metal electrode is equal to the Fermi level of the semiconductor at equilibrium the conduction band edge of the semiconductor needs to be positioned superior to the reduction potential of protons.

For the water splitting to be as efficient as possible a maximum of the solar energy should be exploited. As illustrated in Figure 2.12 the part of the solar irradiation giving the highest power is visible light with wavelengths from 400nm to 800nm. It would therefore be desirable for the bandgap of the photocatalyst to be equivalent to the energy of visible light, i.e. lie between 3.1eV and 1.5eV. This would produce a maximum of excited electron-hole pairs within the semiconductor upon irradiation and yield the highest current output.

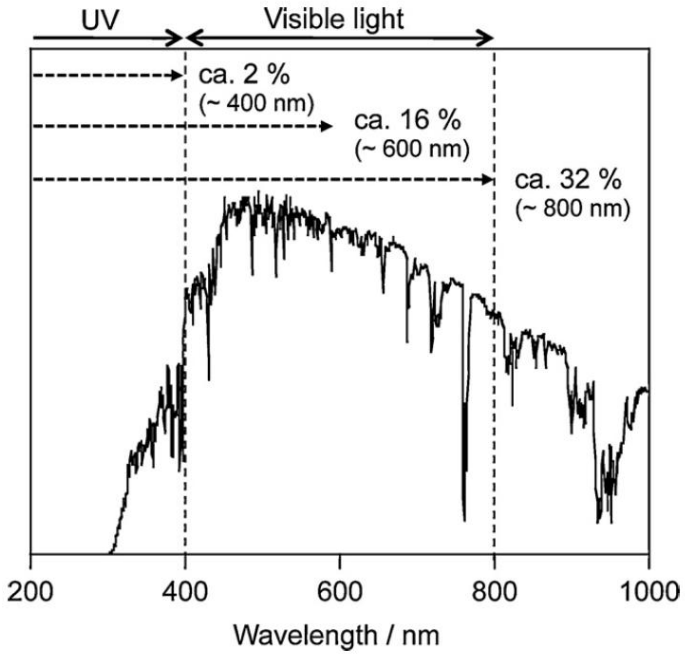

Figure 2.12 : Solar spectrum and maximum solar light conversion efficiencies for water splitting with 100% quantum efficiency [6].

2.3 Electronic structure of $CaNb_2O_6$

Since oxides tend to have oxygen vacancies in the lattice they are usually n-type semiconductors. By applying the Kröger-Vink notation it can be seen that the removal of an oxygen ion with neutral charge at an oxygen lattice site $O_O^{\times}$ produces an oxygen vacancy with double positive charge, $V_O^{\bullet\bullet}$, and donate two electrons to the lattice, reaction (2.28). This corresponds to the standard oxygen reduction reaction.

$$O_O^{\times} \rightarrow V_O^{\bullet\bullet} + 2e' + \frac{1}{2}O_2(g) \tag{2.28}$$

2.3.1 Bandgap

In $CaNb_2O_6$ niobium is present as Nb^{5+} and has a d^0 electron configuration thus a bandgap between the filled p-orbitals and the empty d-orbitals is present. However the major contribution to the valence band formation originates from the 2p-orbitals of oxygen as can be seen in Figure 2.13. The electronic band structure of a semiconductor can be calculated using the density functional theory (DFT), crystal structure parameters and atomic coordinates found in the literature. This has been done for $CaNb_2O_6$ by Cho et al. [26] and a predicted bandgap of 3.72eV was found.

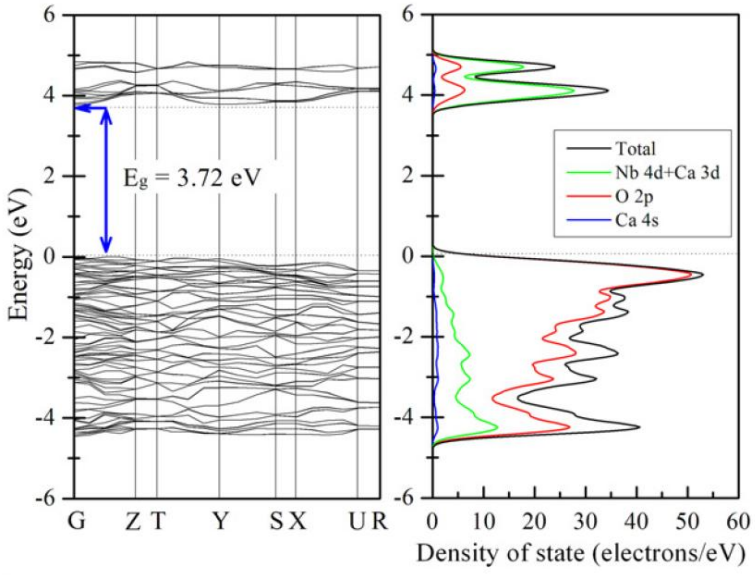

Figure 2.13 : Calculated band structure and density of states for $CaNb_2O_6$ by applying DFT theory and using the CASTEP program [26].

In order to gain insight into the possible electronic transitions in a semiconductor the joint density of states (JDOS) can be calculated [27]. The JDOS is a convolution of occupied valence band DOS, N_V, and empty conduction band DOS, N_C, as shown in equation (2.29). Since interband transitions occur between the two owing to the absorption of light the JDOS represents the absorption spectrum of the material. Nevertheless the JDOS gives equal weight to all possible transitions and it will therefore not reproduce the relative strengths of the optical spectrum.

$$J(\hbar\omega) = \int N_C(E) \cdot N_V(E + \hbar\omega) dE \tag{2.29}$$

2.3.2 Flatband potential

From a careful study of the factors affecting the flatband potential, V_{fb}, Butler and Ginely [23] showed that it could be expressed as:

$$V_{fb} = EA - E_{ref} - \Delta\phi_H - \Delta\phi_{fc} \tag{2.30}$$

Here EA is the semiconductor electron affinity, E_{ref} the reference electrode potential with respect to the vacuum level, $\Delta\Phi_H$ the Helmholtz potential drop due to ions adsorbed on the semiconductor surface and $\Delta\Phi_{fc}$ the difference between the semiconductor Fermi level and the conduction band for n-type semiconductors. For highly doped semiconductors $\Delta\Phi_{fc}$ is typically 0.1eV and can be ignored. When using the SHE as reference electrode E_{ref} is taken to be 4.5eV, see section 2.1.2. The potential drop in the Helmholtz region changes by 59mV/pH-unit as shown in equation (2.15) for metal oxides and will be zero at the PZC. Finally the electron affinity can be calculated from Mulliken electronegativities for each atom, $\chi(atom)$. For an intrinsic semiconducting solid the bulk electronegativity can be assumed to be the geometric mean of the atomic electronegativities of the constituent atoms. Thus for $CaNb_2O_6$ the electron affinity is given by:

$$EA(CaNb_2O_6) = \left[\chi(Ca)\chi^2(Nb)\chi^6(O)\right]^{1/9} - \frac{1}{2}E_g(CaNb_2O_6) \tag{2.31}$$

By applying equation (2.30) the flatband potential of $CaNb_2O_6$ at the PZC can be predicted using Mulliken electronegativities[28] and the theoretical size of the bandgap.

2.4 Characterization techniques

2.4.1 Photocurrent

Dependence on wavelength

The absorption coefficient α of a material is defined by equation (2.32) where *d* is the thickness of the sample and *I* and I_0 is the transmitted and incident light intensities respectively [12]:

$$\alpha = \frac{1}{d}\ln\left(\frac{I_0}{I}\right) \tag{2.32}$$

A relation between the absorption coefficient, the energy of the incident light, $h\nu$, and the bandgap of the semiconductor, E_g, exists and is given by equation (2.33) where *A* and *n* are constants [13]:

$$\alpha = A\frac{(h\nu - E_g)^n}{h\nu} \tag{2.33}$$

When light with energy larger than the bandgap of a semiconductor is absorbed it creates a photocurrent i_{ph} due to the separation of electron-hole pairs in the space charge region of the semiconductor. The photocurrent will therefore be proportional to α by a constant and equation (2.33) can be written in the form of equation (2.34) where *A'* is a constant different from *A*:

$$i_{ph} = A'\frac{(h\nu - E_g)^n}{h\nu} \tag{2.34}$$

The value of the constant *n* reflects the type of transition the electrons undergo. For *n=1/2* the transition is direct and for *n=2* the transition is indirect, see section 2.1.1. Hence by plotting $(i_{ph}h\nu)^{1/n}$ as a function of $h\nu$ both the type of transition and the size of the corresponding bandgap can be determined:

$$\left(i_{ph}h\nu\right)^{\frac{1}{n}} = A'h\nu - A'E_g \tag{2.35}$$

The flatband potential can also be determined from photocurrent measurements. Close to the flatband potential the photocurrent approaches zero as there is no potential gradient in the space charge layer and consequently no separation of electron-hole pairs. Thus by sweeping the potential in the cathodic direction for an n-type semiconductor the photocurrent will disappear close to the flatband potential.

Dependence on voltage

An expression for the total photocurrent density in Schottky junctions (i.e. semiconductor-metal junctions) under monochromatic illumination and reverse bias was derived by Gärtner [29]. Here L is the minority carrier diffusion length and W the width of the space charge layer.

$$i_{ph} = eI_0\left(1 - \frac{e^{-\alpha W}}{1+\alpha L}\right) \tag{2.36}$$

The derivation of the expression is based on the fact that there are two contributions to the total photocurrent. One contribution originates from the carriers generated in the space charge region while the other originates from the diffusion of carriers generated in the bulk into the space charge region. When neglecting limitations due to electrochemical reaction kinetics a semiconductor-electrolyte interface will be similar to a Schottky junction. Accordingly equation (2.36) could be valid for semiconductor-electrolyte junctions as well, as seems to be the case some distance away from the flatband potential [23].

The width of the space charge region W is given by equation (2.37) where W_0 is the depletion layer thickness for a potential drop of 1V across the depletion layer, V_{fb} the flatband potential relative to a reference electrode and V the applied potential relative to the same reference.

$$W = W_0(V - V_{fb})^{1/2} \tag{2.37}$$

From inserting equation (2.37) into equation (2.36) an expression for the photocurrent as a function of the potential is obtained.

$$i_{ph} = eI_0\left(1 - \frac{\exp\left[\alpha W_0(V - V_{fb})^{1/2}\right]}{1+\alpha L}\right) \tag{2.38}$$

As a result a plot of $[ln(i_{ph})]^2$ as a function of potential can be used to determine the flatband potential of the semiconductor. If $\alpha W_0(V\text{-}V_{fb})^{1/2} << 1$ then a plot of the square of the photocurrent versus applied potential will intercept the potential axis at the flatband potential.

2.4.2 Quasi-Fermi level measurements

From the pH dependence of the band edges in a semiconductor, equation (2.15), the quasi-Fermi level of electrons, $E_{F,n}$, can be determined for powder suspensions. Bard et al. [30, 31] introduced a method for measuring the photocurrent of a TiO_2 suspension using a biased collector electrode and enhancing the photocurrent by adding reducible species to the suspension, Figure 2.14. By adding a pH-independent electron acceptor, methyl viologen (MV^{2+}), to the suspension a shift of the Fermi level with pH was observed and the quasi-Fermi level of electrons could be estimated. This method was further developed by Roy et al. [24] who determined the quasi-Fermi level of electrons by measuring the dependence of the photovoltage developed at the collector electrode with pH of the suspension.

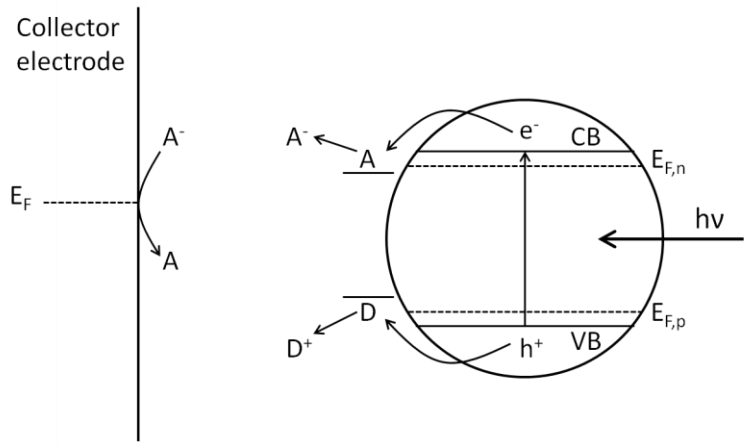

Figure 2.14 : A schematic of reactions at a semiconductor nanoparticle in contact with an electrolyte containing an electron donor D and an electron acceptor A. The formation of A^- in the electrolyte is detected at the biased collector electrode.

In the measurements described above the presence of an efficient hole scavenger in the suspension is indispensable [31]. By removing the photogenerated holes in an irreversible fashion it prevents the formation of O_2 which would compete with the reduction of the electron acceptor. Also it prevents "short circuiting" of the particle from re-oxidation of the electron acceptor at the particle surface.

The choice of hole scavenger is important for obtaining reliable results in both quasi-Fermi level measurements and photocurrent measurements. Several hole scavengers used in the literature have been reported to yield strongly reducing radicals upon one hole oxidation [32]. The radical can then inject an electron into the conduction band and thus complete its oxidation. This is known as current-doubling as it theoretically doubles the carrier generation from that produced by photon absorption. Finally the radical can reduce other species in the electrolyte such as the electron acceptor and thus affect the measured quasi-Fermi level values.

2.4.3 Diffuse reflectance spectroscopy

Generally the total reflectance of a powder surface at any wavelength λ can be considered to be the sum of two components, regular (or specular) reflectance from a plane phase boundary and diffuse reflectance [33]. In a powder where the particles are small compared with the beam cross section and randomly oriented, a part of the incident light will go back at all angles from the surface. This is called diffuse reflection and originates from the reflection, refraction, diffraction, and absorption by the particles. When the particle size is comparable to or smaller than the wavelength of the incident light, the contributions from reflection, refraction and diffraction will be impossible to separate, i.e. scattering occurs. The model proposed by Kubelka and Munk [34] describing the behavior of light travelling inside a light-scattering specimen can then be applied. In the limiting case where the sample is thick enough to ensure that a further increase in thickness will not change the reflectance the Kubelka-Munk (KM) equation becomes [35]:

$$F(R_\infty) = \frac{K}{S} = \frac{(1-R_\infty)^2}{2R_\infty} \tag{2.39}$$

$F(R_\infty)$ is termed the KM or remission function and S and K are the KM scattering and absorption coefficients respectively. The reflectance R_∞ is given by:

$$R_\infty = \frac{R_{sample}}{R_{standard}} \tag{2.40}$$

When a material scatters in a perfectly diffuse manner the KM absorption coefficient K is equal to 2α [35]. If the KM scattering coefficient S is considered as a constant the KM function can be inserted into equation (2.33) yielding equation (2.41) where C is a constant:

$$\left[F(R_\infty)h\nu\right]^{1/n} = C(h\nu - E_g) \tag{2.41}$$

Thus by obtaining $F(R_\infty)$ from equation (2.39) and then plotting $[F(R_\infty)h\nu]^2$ ($n=1/2$) versus $h\nu$ the direct bandgap E_g of the powder sample can be determined. Similarly a plot with $n=2$ would yield the indirect bandgap of the semiconductor powder.

2.4.4 Electrochemical impedance spectroscopy

Electrochemical impedance spectroscopy (EIS) is an experimental method used to characterize an electrochemical system by measuring the impedance, Z, of the system at different frequencies. A small AC sine wave voltage with frequency f and an amplitude of 5-10mV is applied on top of a DC potential. The amplitude and phase of the AC current response of the system is measured relative to the AC component of the applied potential. Hence the impedance is a complex number describing the resistance of the system and is defined as [12]:

$$Z = |Z| e^{j\theta} = \mathrm{Re}(Z) + j\,\mathrm{Im}(Z) \tag{2.42}$$

The amplitude $|Z|$ of the impedance describes the ratio between the amplitude of the AC voltage and the AC current response while θ describes the phase shift of the AC current with respect to the AC voltage.

Different parts of an electrochemical system can be modeled using circuit elements and an equivalent circuit can hence be used to describe the whole system. Impedance measurements can then be employed to determine properties of the circuit elements and subsequently properties of different parts of the electrochemical system. Typical circuit elements used are resistors and capacitors whose impedances are described by:

$$Z_R = R \tag{2.43}$$

$$Z_C = \frac{1}{j\omega C} \tag{2.44}$$

The angular frequency ω is related to the frequency f of the AC sine wave voltage by:

$$\omega = 2\pi f \tag{2.45}$$

The most common equivalent circuit describing an electrochemical system consisting of a semiconductor immerged in an electrolyte is described by a charge transfer resistance R_{ct} in parallel with a space charge capacitor C_{SC} and an electrolyte resistance in series R_S [12]:

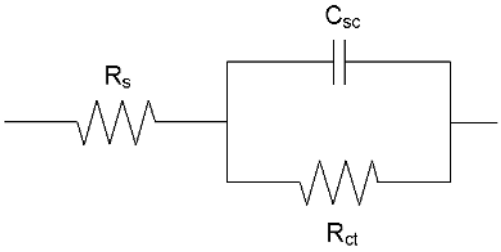

Figure 2.15 : Equivalent circuit for an electrochemical system [12].

The impedance of this equivalent circuit will be a perfect semicircle when plotting the imaginary part of the impedance against the real part for different frequencies ω:

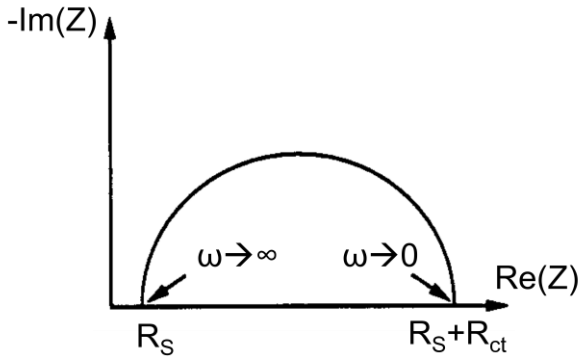

Figure 2.16 : Impedance plot for the equivalent circuit shown in Figure 2.15 [36].

From the impedance plot in Figure 2.16 the values for R_S and R_{ct} can be determined since the space charge capacitor will act as open circuit at low frequencies ($\omega \rightarrow 0$) and short circuit at high frequencies ($\omega \rightarrow \infty$) as can be seen from equation (2.44). The low frequency intercept with the real axis is thus equal to R_S+R_{ct} and the high frequency intercept corresponds to R_S. At high frequencies the equivalent circuit can be represented as in Figure 2.17 where the charge transfer resistance in parallel with the capacitor is neglected.

Figure 2.17 : Equivalent circuit from Figure 2.16 at high frequencies.

A plot of the imaginary part of the impedance versus the real part of the equivalent circuit in Figure 2.17 will give a line parallel to the y-axis as shown below:

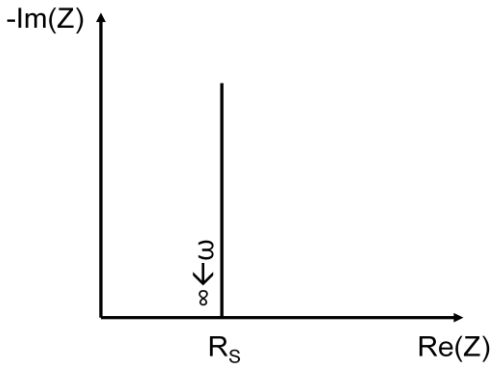

Figure 2.18 : Impedance plot for the equivalent circuit in Figure 2.17.

The capacitance of the semiconductor at high frequencies can then be determined from the imaginary part of impedance using equation (2.46).

$$C = -\frac{1}{\omega \,\mathrm{Im}(Z)} \tag{2.46}$$

2.4.5 Mott-Schottky plot

The potential and charge distribution within the space charge region of a semiconductor surface is determined by the Poisson equation [18] as mentioned in section 2.1.3. Here $\rho(x)$ represents the charge density at a distance x from the surface, ε the dielectric constant and ε_0 the permittivity of vacuum:

$$\frac{d^2 \Delta\phi_{SC}}{dx^2} = -\frac{\rho(x)}{\varepsilon\varepsilon_0} \tag{2.47}$$

By solving the Poisson equation a differential capacitance of the space charge region can be deduced, and for doped semiconductors the Mott-Schottky equation is obtained [19]:

$$\frac{1}{C_{SC}^2} = \frac{2}{e\varepsilon\varepsilon_0 n_0}\left[\Delta\phi_{SC} - \frac{kT}{e}\right] \tag{2.48}$$

This linear relation between $1/C_{SC}^2$ and $\Delta\Phi_{SC}$ can be applied for simplified cases where there are no surface states present at the semiconductor-electrolyte interface. A sufficiently concentrated redox electrolyte also needs to be assumed in order to neglect the potential drop across the Gouy layer.

Since the space charge capacitance and the capacitance describing the Helmholtz double layer are in series, the total capacitance C of the system will be:

$$\frac{1}{C} = \frac{1}{C_{SC}} + \frac{1}{C_H} \tag{2.49}$$

If $C_{SC} << C_H$, which is generally the case for moderately doped semiconductors under depletion conditions, the contribution from C_H on the total capacitance will be small and can be neglected [19]. Thus a change in the potential drop across the interface by changing the electrode potential V will mainly result in a change of the potential drop in the space charge region, V_{SC}. The flatband potential can consequently be described by:

$$\Delta\phi_{SC} = V - V_{fb} \tag{2.50}$$

An extrapolation of the Mott-Schottky plot to $1/C_{SC}^2 \to 0$ yields the potential at which $\Delta\phi_{SC} \to 0$ since the thickness of the space charge layer, d_{SC}, is inverse proportional with the capacitance and approaches zero [12]:

$$d_{SC} = \frac{\varepsilon\varepsilon_0}{C_{SC}} \tag{2.51}$$

Accordingly an extrapolation to $1/C_{SC}^2 = 0$ gives $V \approx V_{fb}$ when *kT/e* is small. However specific adsorption and other processes at the semiconductor-electrolyte interface will influence the flatband potential. Therefore the flatband potential only reflects the situation in situ for a given set of conditions of the semiconductor-redox electrolyte such as pH, redox couple and redox concentrations.

3 Experimental

Ion distilled water of Milli-Q quality (ultrapure) was used to prepare all solutions and wash all glass ware before use. For the powder preparation the glass ware was also washed in a boiling peroxide bath prior to application.

3.1 Preparation of $CaNb_2O_6$

The $CaNb_2O_6$ powder used in this project was prepared by PhD candidate Morten Tjelta as part of the work on his PhD thesis [37]. Therefore only a short description of the method is included in this report.

The powder was prepared using a sol-gel method. Stoichiometric amounts of the precursors, a niobium malic acid complex and a calcium EDTA complex, were mixed. Addition of ethylene glycol resulted in a condensation polymerization and a gel was formed. The gel was dried and calcined at 900°C resulting in a white powder of $CaNb_2O_6$. A particle analysis was performed using a particle analyzer (Delsa Nano C Particle analyzer, Beckmal Coulter) combined with an auto titrator (Delsa Nano AT Auto titrator, Beckmal Coulter), and approximately 300nm particle agglomerates with a PZC equal to 3 were detected.

3.2 Doping with nitrogen

Doping of $CaNb_2O_6$ with nitrogen was done by exposing the powder to an ammonia atmosphere at elevated temperatures. A small amount of pure $CaNb_2O_6$ was placed in a quartz crucible and then placed inside a tube furnace (Lenton LTF 12/50/300). The furnace was connected to a gas inlet and argon gas was blown through the system prior to heating. Dry ammonia gas (anhydrous ammonia, YaraProxair) was used as nitrogen source and was blown through the furnace during heating of the furnace, for 2 hours at the desired temperature (500, 600, and 700°C), and during cooling down to 300°C. The used ammonia gas was collected by bubbling it through water. The nitrogen doped samples will hereafter be referred to as N700, N600 and N500 for nitrogen doping of $CaNb_2O_6$ at 700°C, 600°C and, 500°C respectively.

3.3 X-ray diffraction

X-ray diffraction (XRD) was performed to examine the phase composition of pure and nitrogen doped $CaNb_2O_6$. For the pure oxide the powder X-ray diffractometer used was an AXS D8Focus while for the nitrogen doped samples a Siemens D5000 was used. The scans were recorded for 2θ ranging from 10-90° with a step size of 0.02° and a counting time of 0.5s for pure $CaNb_2O_6$ and a step size of 0.016° and a counting time of 1s for the N-doped

powders. Rotation of the sample holder was applied during all the scans. A silicon single crystal was used as sample holder and the samples were prepared by dispersing the powder in ethanol before transferring it to the silicon substrate.

3.4 Diffuse reflectance spectroscopy

Diffuse reflectance spectroscopy (DRS) was used to examine the absorption properties of the photocatalyst powders and hence determine their bandgap using the Kubelka-Munk relation, section 2.4.3. An xenon lamp (300W, Newport) was connected to an integrating sphere (AvaSphere-50-REFL, 50mm internal diameter, 10mm sample port diameter), by an optical illumination fiber. A simple illustration of the integrating sphere is shown in Figure 3.1.

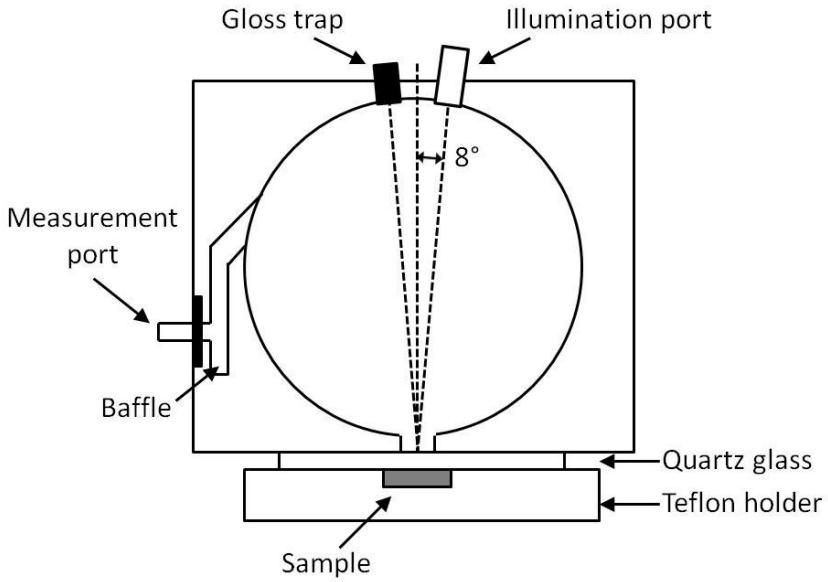

Figure 3.1 : The basic principles of the reflection integrating sphere.

The powder to be examined was placed in a sample holder made of PTFE (Teflon®) with a quartz glass used as cover. A cover was used to avoid getting powder into the sphere and affect the reflection properties of the sphere. White light illuminated the sample directly via an illumination port tilted 8 degrees with respect to the sample. The integrating sphere was equipped with a gloss trap (AvaSphere-GT50) to exclude specular reflections from the measurement. Diffuse reflected light from the sample was integrated in the sphere and collected by a baffle. It was then sent to a fiber optic spectrometer (AvaSpec-2048) through the measurement port by an optical read fiber. The reflection spectra with respect to a reference (Avantes reference tile, WS-2, diffuse PTFE material) were measured by the spectrometer and processed in the program "AvaSoft 7.4".

3.5 Electrochemical and photoelectrochemical measurements

A standard three electrode setup was used for the electrochemical measurements with the photocatalyst on a conducting substrate as working electrode (WE), platina as counter electrode (CE) and a reversible hydrogen electrode (RHE) as reference. The reference electrode (RE) was placed as close to the working electrode as possible to reduce ohmic losses in the electrolyte. A sketch of the setup is illustrated in Figure 3.2.

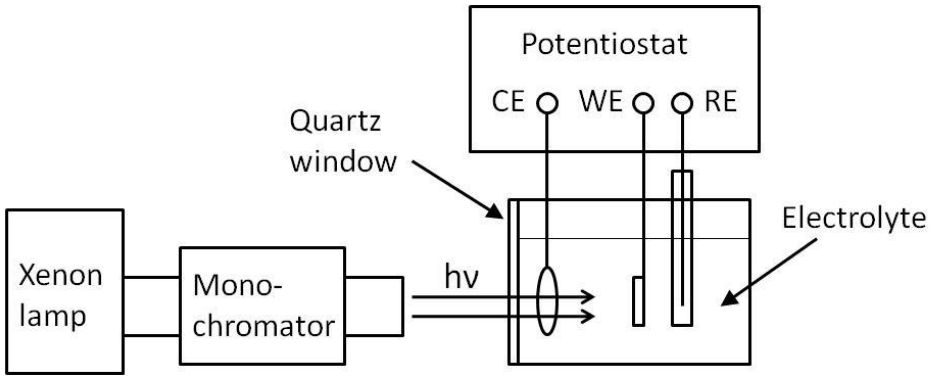

Figure 3.2 : Experimental setup consisting of a standard 3 electrode setup connected to a potentiostat with a xenon lamp irradiating the working electrode.

The electrodes were connected to a potentiostat (Zahner IM6ex) and placed in a square shaped cell with one side made of quartz. The light was sent through the plane quartz side to reduce the refraction and absorption of light in the cell wall. As electrolyte 0.5M H_2SO_4 (95-97%, Sigma-Aldrich) or 0.5M K_2SO_4 (99.0%, Alfa Aesar) was used. The current and potential were measured and regulated using the program "Thales". All the polarizing potentials reported in this report are referred to the standard hydrogen electrode.

An xenon lamp (300W, Newport) connected to a monochromator (Oriel Cornerstone™ 260 1/4m, Newport) was used as a light source and gave monochromatic light at the desired wavelength (±5nm). It was possible to control the time and wavelength of irradiation upon the sample with an automatic chopper and the program "Monochromator".

3.5.1 The working electrode

The working electrode consisted of a photocatalyst film on a conducting substrate. Several different substrates and methods for the electrode preparation were employed. The parts of the electrode surface that were not covered with the photocatalyst film were isolated with nail polish in order to reduce the background currents.

Electrodes of HOPG (highly ordered pyrolytic graphite) and GC (glassy carbon) were made by attaching a Pt (platina) wire to the back of 1cm^2 sized electrodes using a silver-suspension (Pelco® colloidal silver liquid, Ted Pella Inc.) and aluminum adhesive tape. The electrodes were then put on a hot plate at 90°C and a suspension of photocatalyst particles was sprayed onto the electrode as evenly as possible using an airbrush. The suspensions consisted of 5mg photocatalyst powder and 6mL ethanol. In order to make the suspensions homogeneous they were put in an ultrasonic bath for at least 30min prior to use. The GC electrode was cleaned with ethanol before spraying whereas a graphite layer was removed using scotch tape for the HOPG electrode.

Thick films of the photocatalyst were prepared by mixing 20mg catalyst powder with 50µL tergitol (nonionic surfactant, type 15-S-5, Sigma) and 40µL ethanol. The suspension was put in an ultrasonic bath for approximately 30min and then placed on a conducting substrate such as Pt or float glass with a thin ITO (indium tin oxide) layer. The film was dried in a heating cabinet at 80°C and thereafter heated for 2 hours at 700°C for Pt and 500°C for ITO in a tube furnace (Carbolite CTF 12/65/550) under a synthetic air atmosphere.

3.5.2 Photocurrent measurements

The photocurrent measurements were performed at constant anodic potentials. A photoresponse of the catalyst was measured by irradiating the working electrode with monochromatic or white light. The light was turned on and off in intervals using a chopper and the corresponding current was measured by the potentiostat. By varying the wavelength of the light from 200nm to 700nm using intervals of 5nm lasting 5seconds each, a wavelength dependent photocurrent was measured. As the different wavelengths had different intensities the photocurrent measurements had to be normalized. The intensity of the light at different wavelengths was measured using an optical intensity measurer (model 1815-C, Newport).

Experiments were also performed with acetic acid as a hole scavenger in the electrolyte in an attempt to increase the photocurrent response. Thus 9vol% acetic acid (99-100% Puriss, KEBO lab) was added and the electrolyte stirred for some minutes before further measurements.

3.5.3 Quasi-Fermi level measurements

A suspension was made by adding 20mg $CaNb_2O_6$ powder to 40mL 0.5M KNO_3 (99%, Merck) and 5mol% acetic acid (99-100% Puriss, KEBO lab). An ultrasonic bath was used for minimum 30min to obtain a stable suspension. The suspension was placed in a cell made of quartz together with a large Pt counter electrode, RHE reference and a small Pt working electrode. Argon gas was bubbled through the solution for about 30min to remove dissolved oxygen. The suspension was irradiated by both monochromatic and white light under anodic polarization of the working electrode. Measurements were done both with and without stirring

of the electrolyte, and with the addition of 1mmol of a Ru(III) complex (hexaammineruthenium(III)chloride, Aldrich Chemistry) as an electron scavenger. A sketch of the electrochemical cell used during the experiments is shown in Figure 3.3.

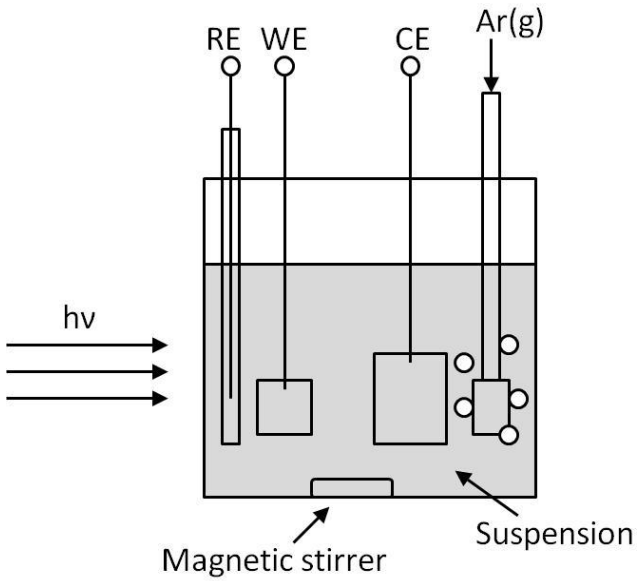

Figure 3.3 : A simple illustration of the experimental setup used for quasi-Fermi level measurements.

3.5.4 Electrochemical impedance spectroscopy

A potentiostat (Zahner IM6ex) was used to carry out the impedance measurements. The impedance was measured at potentials ranging from 0 to 1.2V by applying a 10mV AC-voltage with frequencies from 100 mHz – 100 kHz onto the constant potential. The amplitude and phase of the corresponding AC-current was measured by the potentiostat. Impedance data were used to determine the capacitance of the space charge region of the photocatalyst by modeling the electrochemical system as a simple equivalent circuit, see Figure 2.17 in section 2.4.4. The capacitance could then be used in Mott-Schottky plots, section 2.4.5, in order to determine the flatband potential of the photocatalyst.

4 Results

4.1 Doping with nitrogen

A color change of the $CaNb_2O_6$ powder was observed from the doping with nitrogen. The change was directly related to the temperature used during the heat treatment as shown in Figure 4.1. Doping at higher temperatures yielded a darker color than doping at lower temperatures. The powder doped at 700°C (N700) was almost black, the powder obtained at 600°C (N600) grey, while the powder from doping at 500°C (N500) was bright grey.

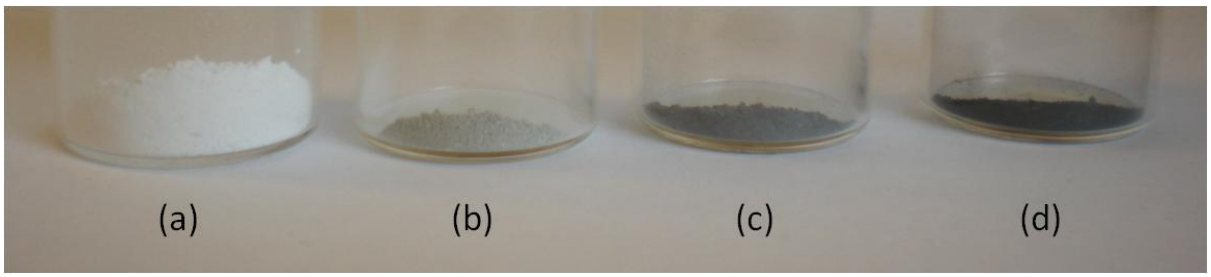

Figure 4.1 : Powders doped with nitrogen at different temperatures: (a) pure $CaNb_2O_6$, (b) 500°C, (c) 600°C and (d) 700°C.

4.1.1 X-ray diffraction

In order to investigate the phases present in the oxide before and after doping with nitrogen XRD scans were recorded, Figure 4.2. All the intensity peaks for the undoped $CaNb_2O_6$ powder were identified as a pure orthorhombic phase of $CaNb_2O_6$ except for the two small peaks marked with black circles. These were identified as Nb_2O_5, one of the precursors used in the synthesis of $CaNb_2O_6$. Furthermore all of the nitrogen doped samples exhibited a homogeneous orthorhombic phase equivalent to pure $CaNb_2O_6$. Hence no impurity phases seemed to appear due to the nitridation process.

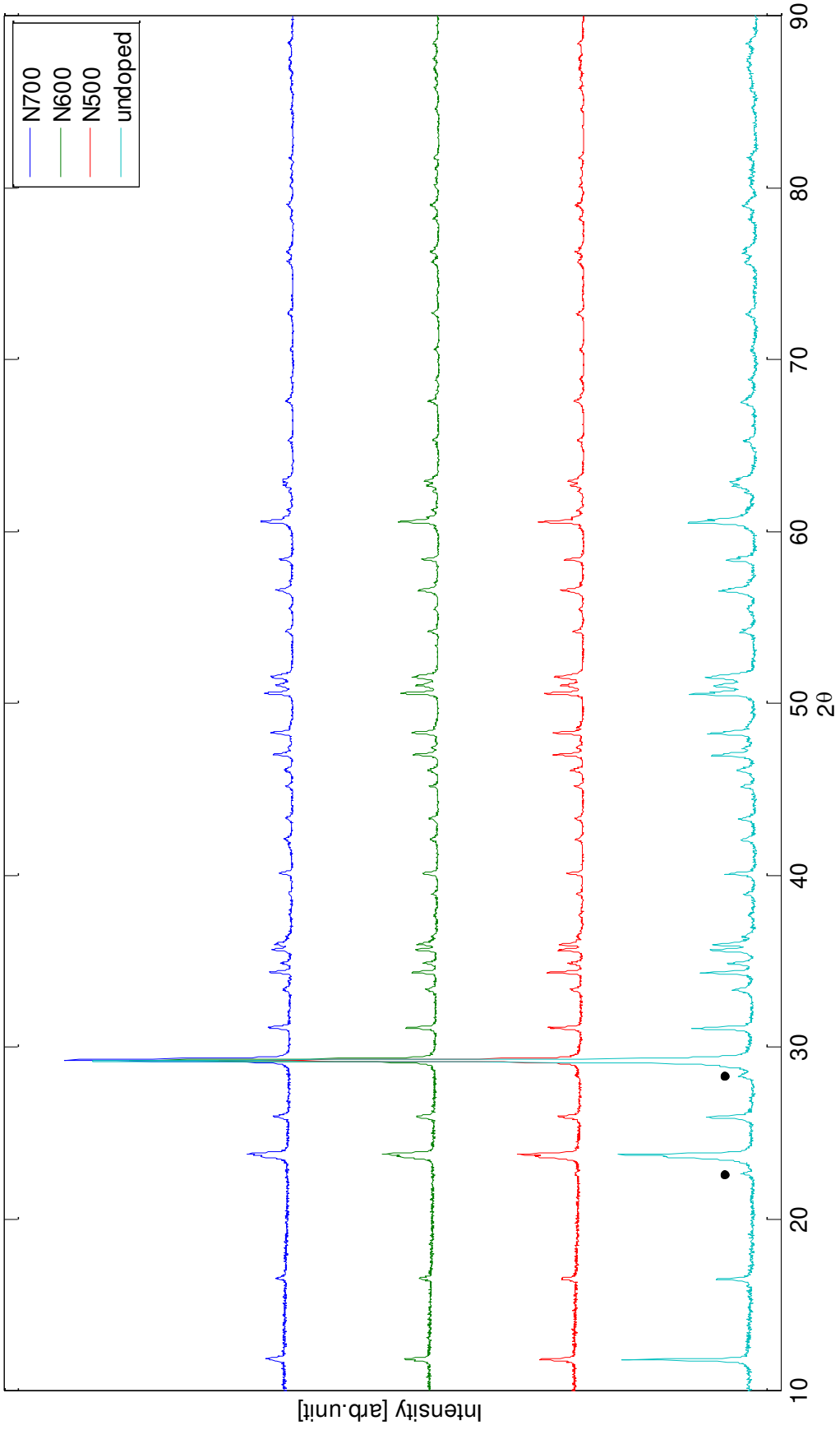

Figure 4.2 : XRD spectra of pure and nitrogen doped $CaNb_2O_6$.

4.2 Theoretical calculations

Density functional theory (DFT) was used as a theoretical approach to determine the electronic structure of pure and nitrogen-doped $CaNb_2O_6$. The calculations were performed by Postdoc Sverre Magnus Selbach using the generalized gradient approximation (GGA). The predicted value for the bandgap of the pure photocatalyst was found to be 3.85eV as shown in Figure 4.3.

By substituting an oxygen atom in the lattice with a nitrogen atom DFT calculations could also predict the density of states and bandgap of nitrogen-doped $CaNb_2O_6$. The result is shown in Figure 4.4 yielding a theoretical bandgap of 3.05eV for the N-doped oxide. A narrowing of the bandgap for the N-doped $CaNb_2O_6$ seems to be due to the formation of intermediate bands just above the valence band. The bands appear to be shifted to lower energies in the calculations for the N-doped oxide. This is merely due to the choice of reference used in the calculations and does not affect the distribution of the bands.

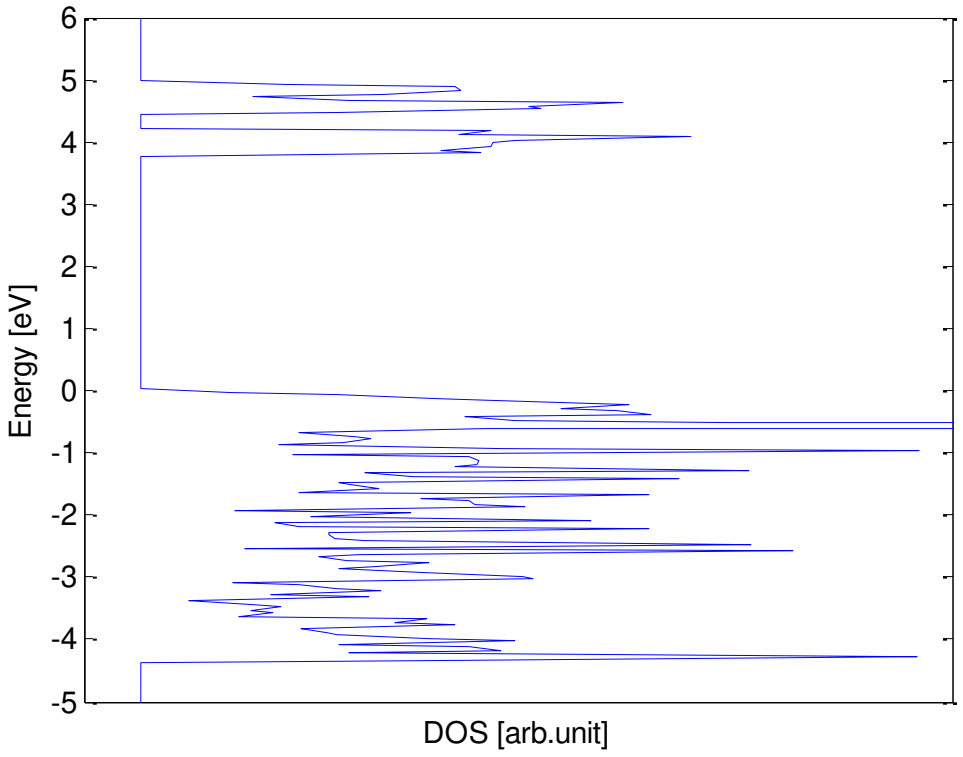

Figure 4.3 : DFT calculations showing the density of states for undoped $CaNb_2O_6$.

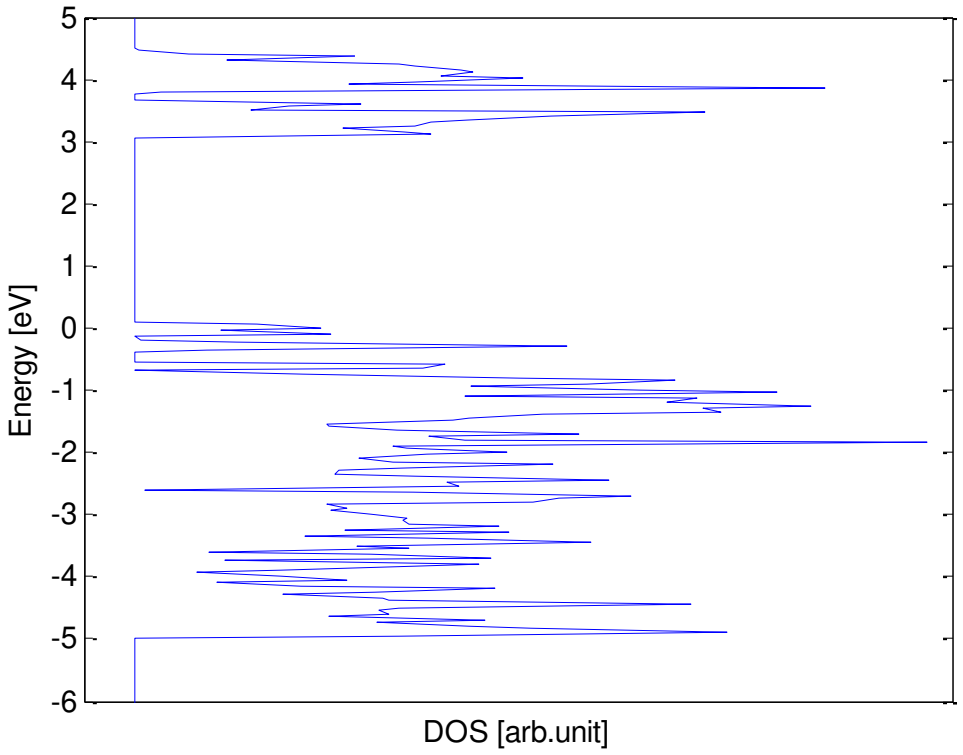

Figure 4.4 : DFT calculations showing the density of states for N-doped $CaNb_2O_6$.

Further theoretical investigations of the light absorption in the photocatalyst were done by calculating the JDOS according to equation (2.29). The results are illustrated for pure and nitrogen-doped $CaNb_2O_6$ in Figure 4.5 and Figure 4.6 respectively. The N-doped oxide showed increased absorption of photon energies in the visible light region compared to the pure oxide.

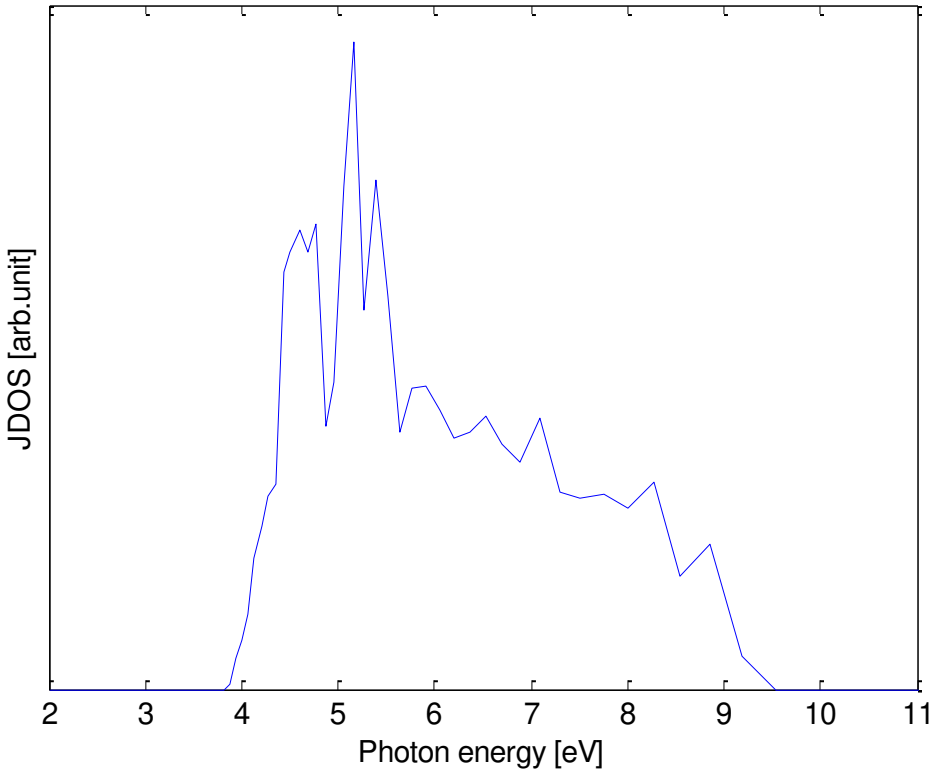

Figure 4.5 : Joint density of states for $CaNb_2O_6$.

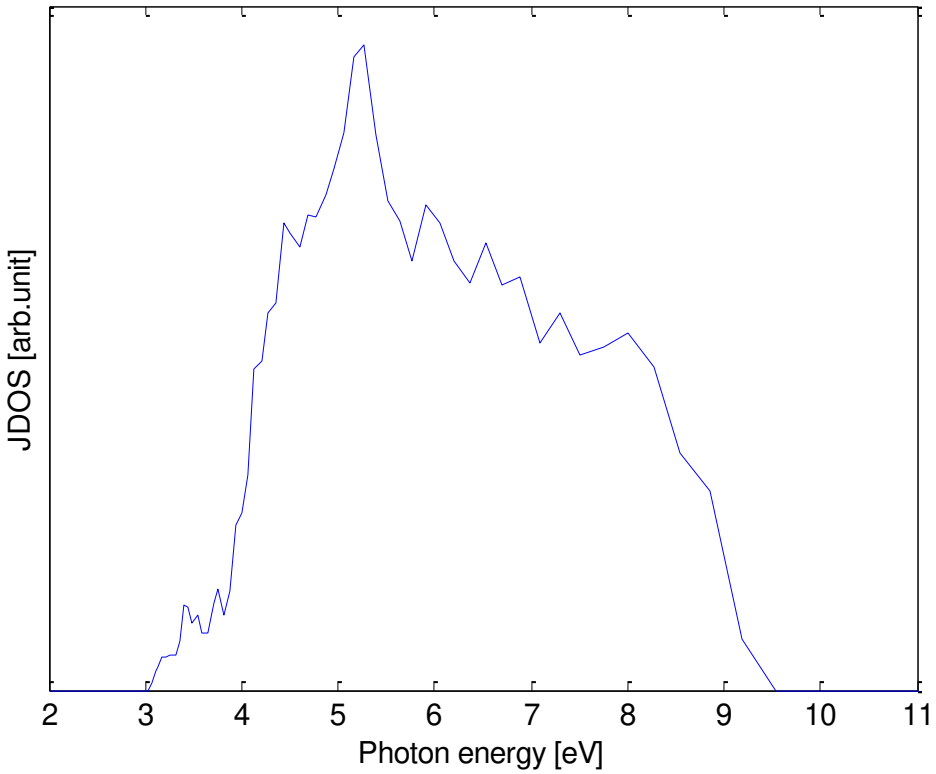

Figure 4.6 : Joint density of states for N-doped $CaNb_2O_6$.

Finally a theoretical consideration of the flatband potential of $CaNb_2O_6$ was done by calculating the electron affinity of $CaNb_2O_6$ at the PZC. Equation (2.31) was used by inserting Mulliken electronegativities given by Putz [28]. Both the values computed by Putz and experimental values reported by Putz were used and yielded different values for the electron affinity. By inserting the calculated electron affinity and the theoretical bandgap of 3.85eV into the expression for the flatband potential developed by Butler and Ginley [23], equation (2.30), the theoretical flatband potential of $CaNb_2O_6$ was obtained. Using experimental values of the electronegativity yielded a flatband potential of -0.72eV while the values computed by Putz gave a flatband potential of 0.14eV.

A theoretical energy level diagram could then be constructed for $CaNb_2O_6$ and related to the reduction potential of protons and oxidation potential of water as shown in Figure 4.7.

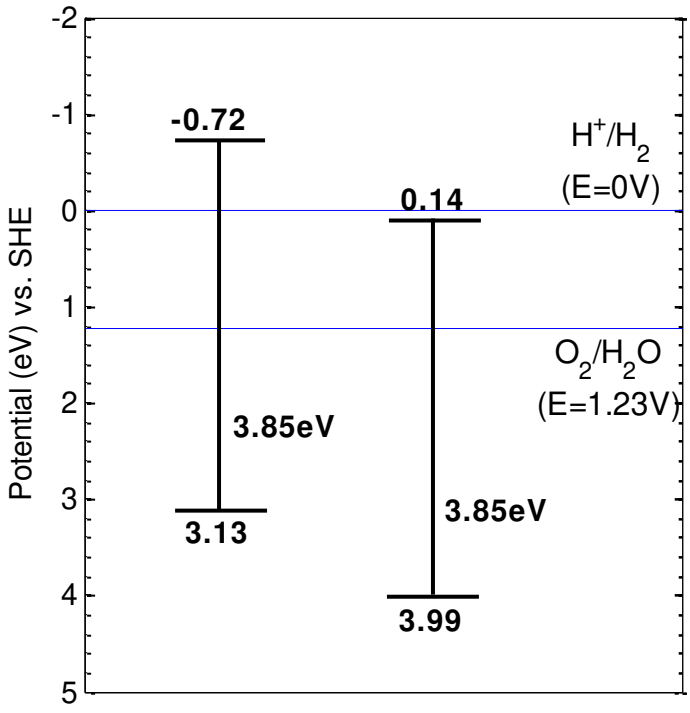

Figure 4.7 : Theoretical energy band diagram for $CaNb_2O_6$ using experimental values (left) and calculated values (right) of the Mulliken electronegativity as reported by Putz [28].

4.3 Diffuse reflectance spectroscopy

Diffuse reflectance spectroscopy was employed to investigate the absorption properties of both pure and nitrogen doped $CaNb_2O_6$. By irradiating the samples with white light and collecting the diffuse reflectance using an integrating sphere the reflectance with respect to a PTFE reference tile were obtained as shown in Figure 4.8.

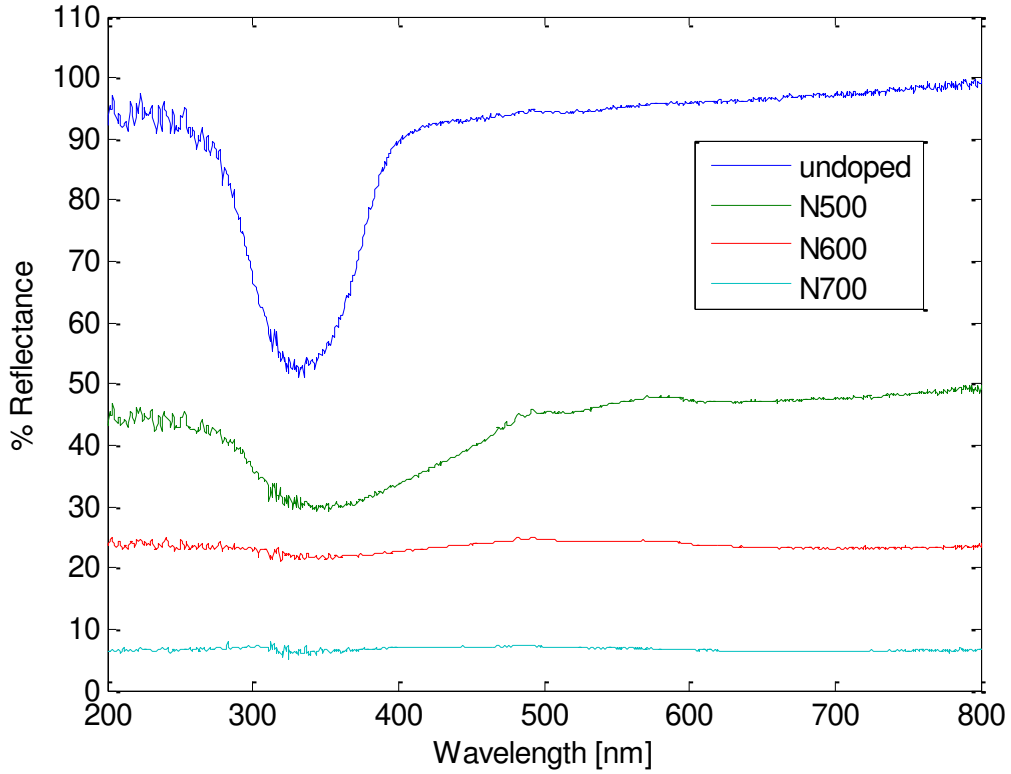

Figure 4.8 : Diffuse reflectance spectra obtained by irradiating the photocatalyst powder with white light and using a PTFE tile as reference.

Undoped $CaNb_2O_6$ absorbed light with wavelengths from 250-400nm as can be seen from the large drop in reflectance at these wavelengths. Similarly the sample doped with nitrogen at 500°C showed a drop in reflectance and absorbed light from 250-470nm. The two samples doped with nitrogen at 600°C and 700°C reflected only a small amount of light and no decrease in reflection for specific wavelengths was detected.

A method for determining the bandgap of semiconductor powders is to apply the Kubelka-Munk theory to diffuse reflectance measurements, hence make a plot of $[F(R_\infty)hv]^{1/n}$ versus hv as described in section 2.4.3. This was done for the two samples showing a distinct drop in diffuse reflectance, the undoped oxide and the powder doped with nitrogen at 500°C. Figure 4.9 and Figure 4.10 represent direct bandgap plots ($n=1/2$) while Figure 4.11 shows a plot for indirect bandgap determination ($n=2$). From extrapolation of the linear regions the bandgaps of the powders could be determined from the intersect with the x-axis according to

equation(2.41). This yielded direct bandgaps of approximately 3.4eV and 2.7eV for $CaNb_2O_6$ and N500 respectively. Indirect bandgaps of 3.1eV and 1.4eV were also determined.

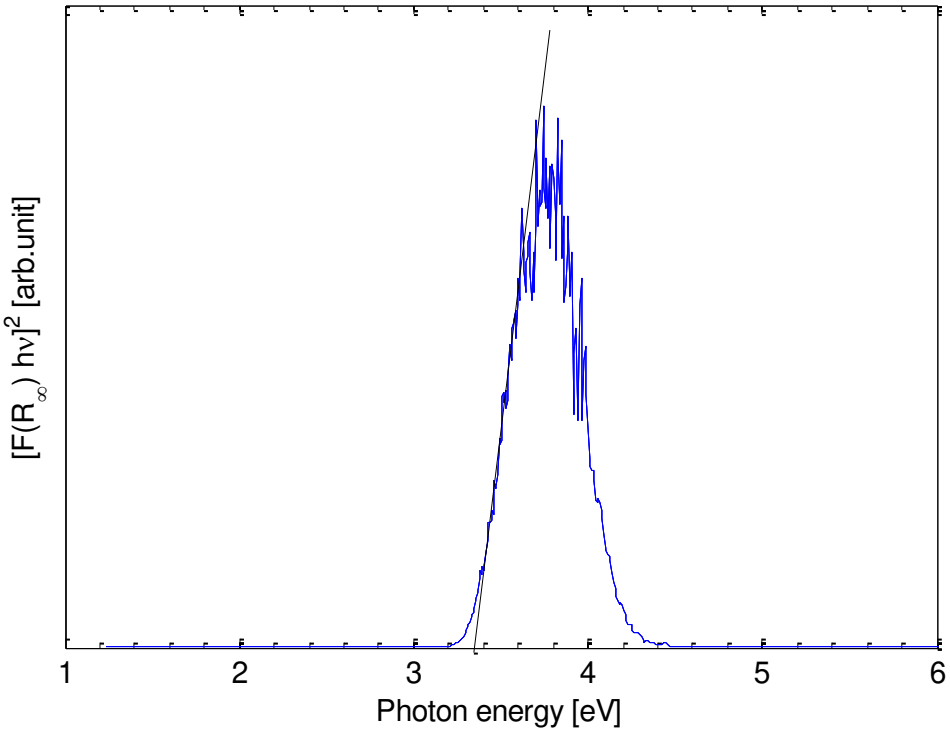

Figure 4.9 : Kubelka-Munk transformed reflectance spectra for $CaNb_2O_6$ yielding a direct bandgap of 3.4eV.

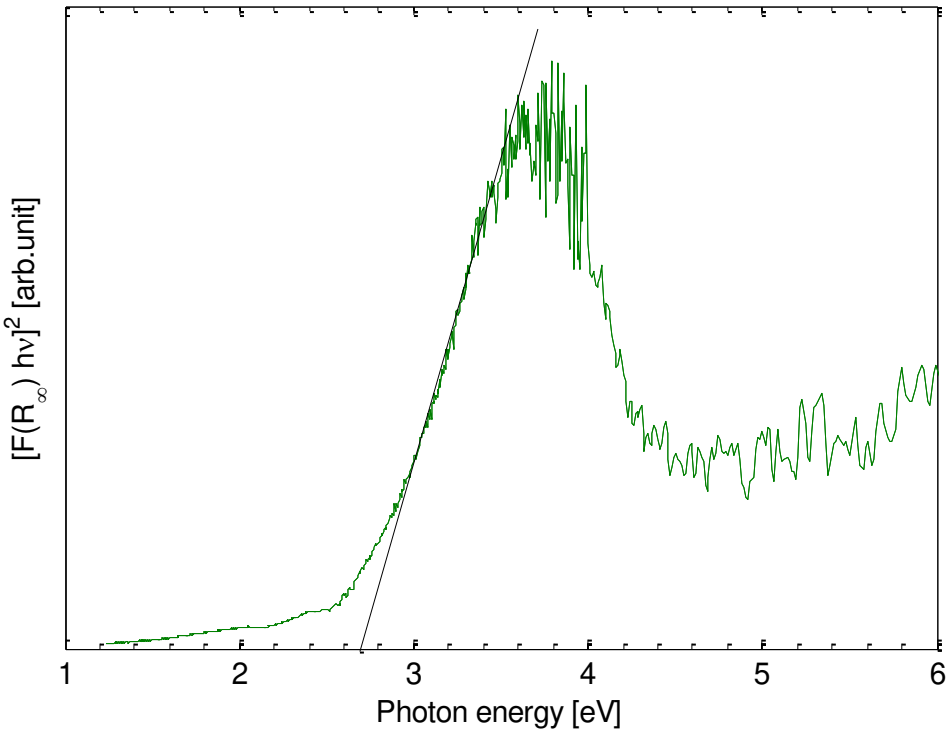

Figure 4.10 : Kubelka-Munk transformed reflectance spectrum for N500 yielding a direct bandgap of 2.7eV.

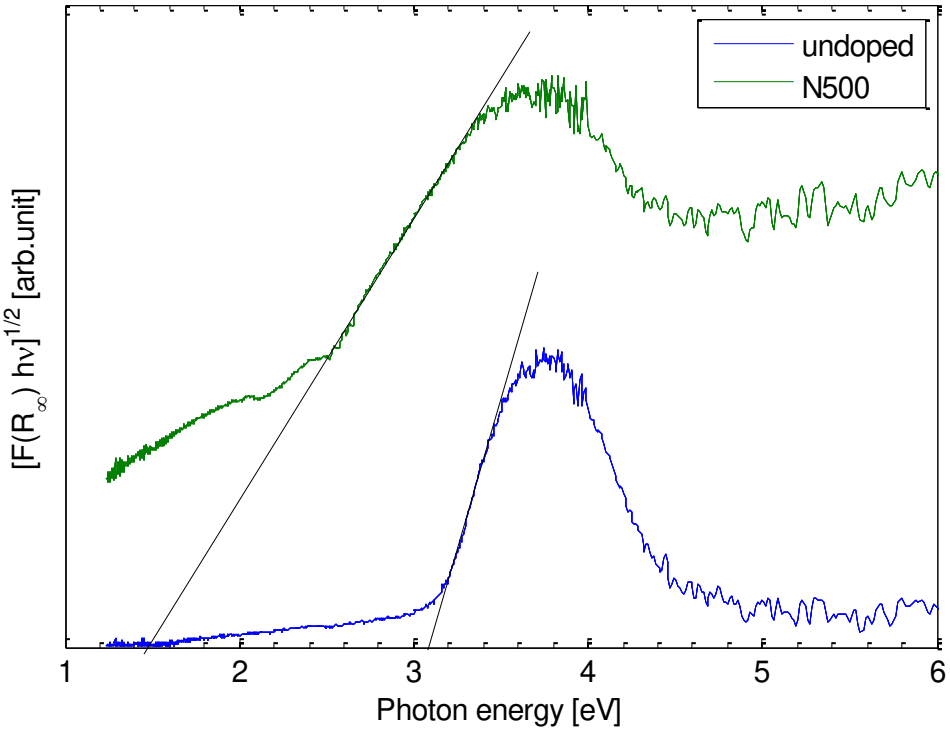

Figure 4.11 : Kubelka-Munk transformed reflectance spectra for n=2 giving indirect bandgaps of 3.1eV and 1.4eV for undoped $CaNb_2O_6$ and N500 respectively.

4.4 Photocurrent measurements

In order to perform electrochemical measurements on the photocatalyst powder electrodes had to be prepared. Several different substrate materials were employed since challenges with adhesion of the powder, coverage of the substrate surface, and photoresponse from the substrate were frequently encountered. Therefore all of the substrates used were investigated both with and without the photocatalyst in order to ensure that the observed responses originated from the photocatalyst and not the substrate. Carbon paper and glassy carbon were found to yield minor photocurrents, but these were negligible compared to the photoresponse with a photocatalyst layer deposited on the surface. On the other hand ITO gave a high photocurrent under illumination and the small photocurrent measured on a $CaNb_2O_6$ thick film originated most likely from the substrate. Only the Pt and HOPG substrates did not yield any photocurrents when illuminated. However the background currents were often so high that a photocurrent from the photocatalyst powder was not detectable.

4.4.1 Photocurrent transients

The measured photocurrent appeared to be time dependent and yielded similar photocurrent transients for both the undoped and N-doped $CaNb_2O_6$. A typical photoresponse for a sample irradiated with 300nm monochromatic light while polarized at a high anodic potential is shown in Figure 4.12. Clearly the photocurrent onset is fast while it takes some time for the photocurrent to reach a stable value. Slow transients were also observed when the light was turned off.

In addition cathodic photocurrents were observed when applying low anodic potentials to the working electrode, Figure 4.13. The corresponding transients increased anodically with time, hence the cathodic current decreased. When the light was turned off the cathodic background current did not increase again, but continued to decrease.

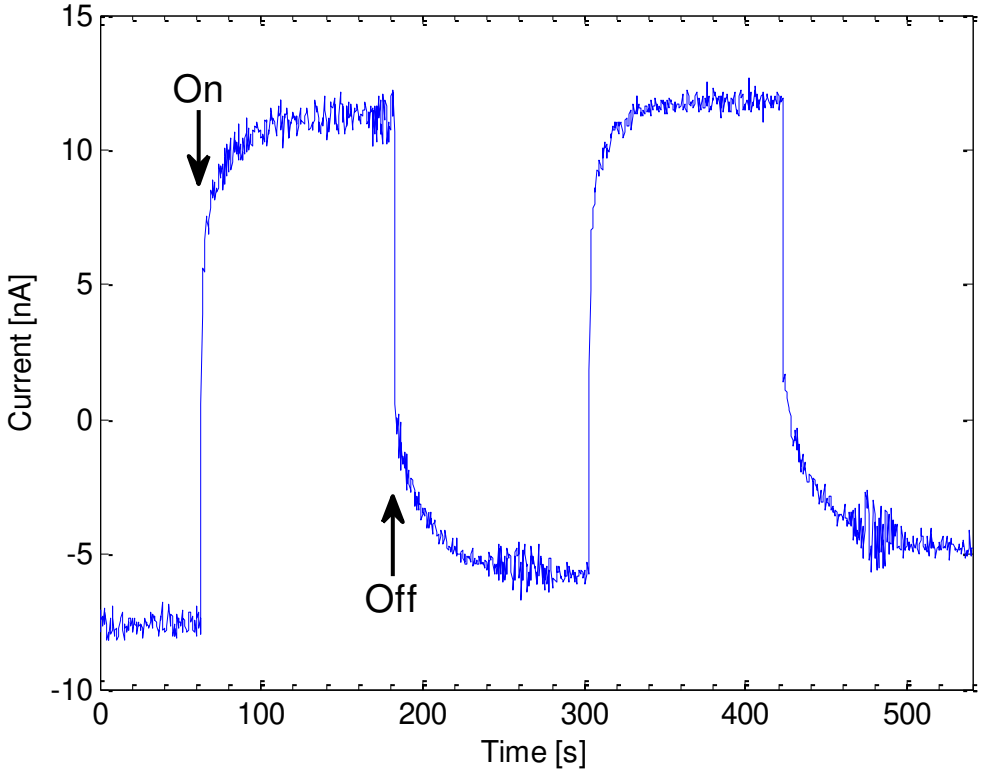

Figure 4.12 : Photoresponse for N500 on HOPG polarized at 800mV and irradiated by 300nm monochromatic light.

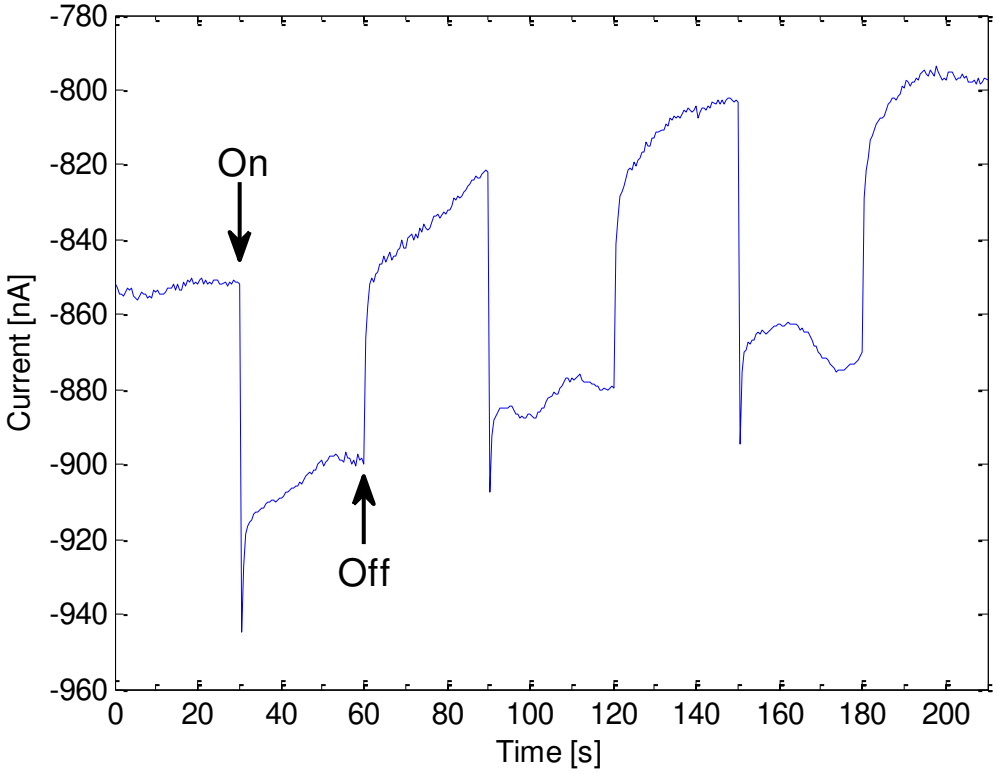

Figure 4.13 : Photoresponse for N500 on HOPG polarized at 100mV and irradiated by 300nm monochromatic light.

4.4.2 Wavelength dependence

The optical properties of pure and nitrogen doped $CaNb_2O_6$ were investigated by irradiating the photocatalyst with monochromatic light from 200-700nm and measuring the corresponding photocurrent termed i_{ph}. In all the measurements the background current was modelled as a straight line and subtracted from the measured values. Additionally the measurements were corrected for differences in intensity for the different wavelengths of the light by normalizing with respect to the highest intensity. A plot of the intensity vs. wavelength is shown in Figure 4.14. Because of the low intensities for wavelengths below 250nm the photocurrent measurements were quite unstable in this region and are not included in the photocurrent graphs.

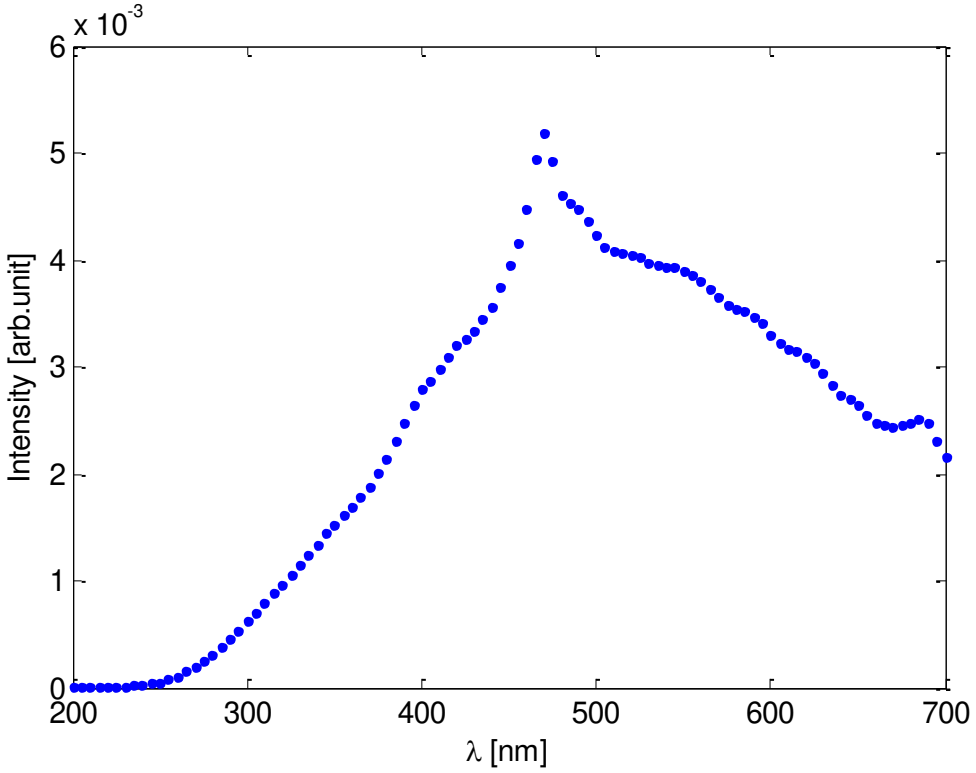

Figure 4.14 : The measured intensity for different wavelengths of the monochromatic light.

Photocurrents for undoped $CaNb_2O_6$ has already been investigated in a project work performed at NTNU in the fall 2011 [38], these plots are not included here. Nevertheless the N500 powder showed the same photocurrent characteristics as the undoped $CaNb_2O_6$ and Figure 4.15 can hence represent both samples. In accordance with the project work a direct bandgap of 3.7eV and an indirect bandgap of 3.4eV were determined by plotting $(i_{ph}hv)^{1/n}$ vs. the photon energy and extrapolating the linear region as described in section 2.4.1, see Figure 4.16 and Figure 4.17.

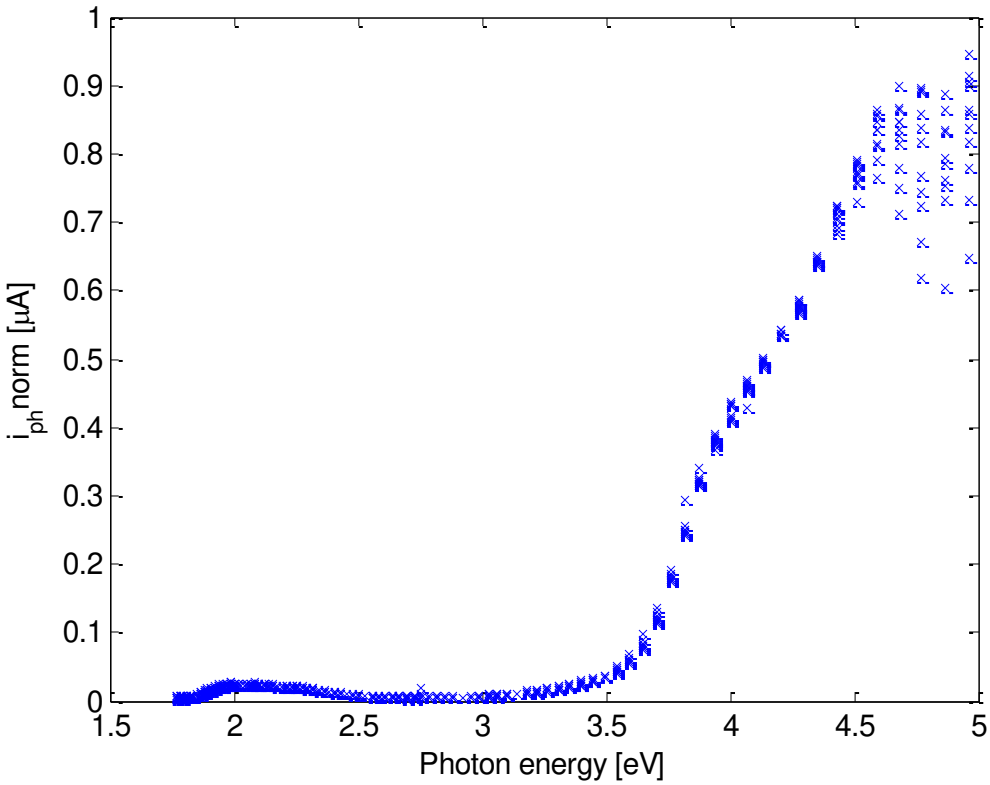

Figure 4.15 : Normalized photocurrent for N500 on HOPG polarized at1.2V.

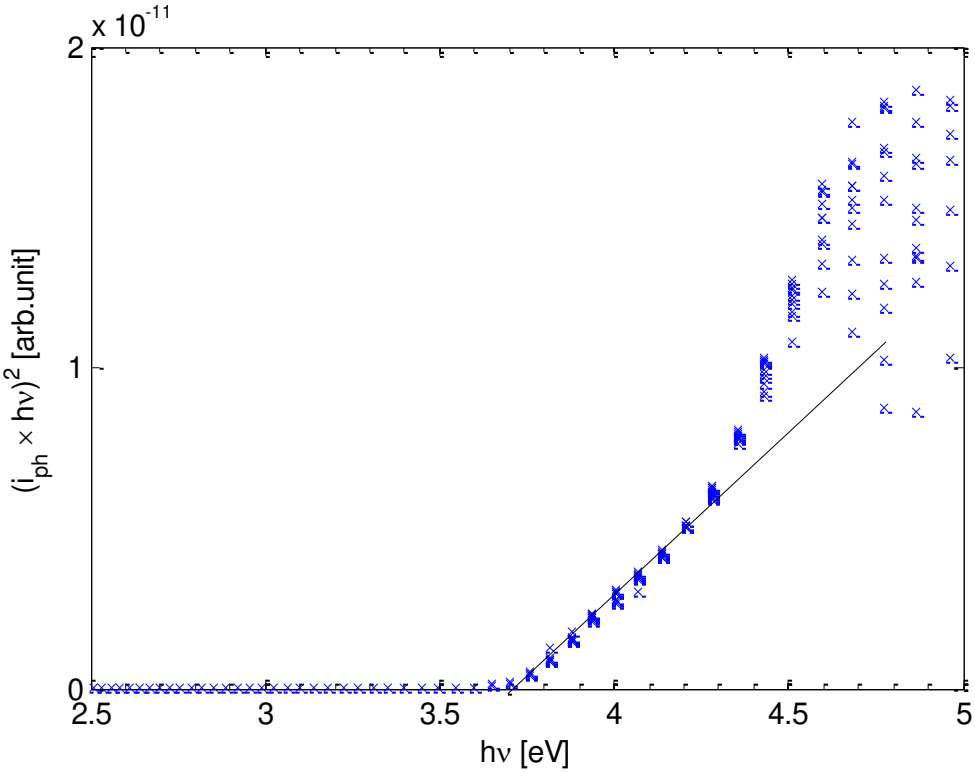

Figure 4.16 : Direct bandgap for N500 on HOPG.

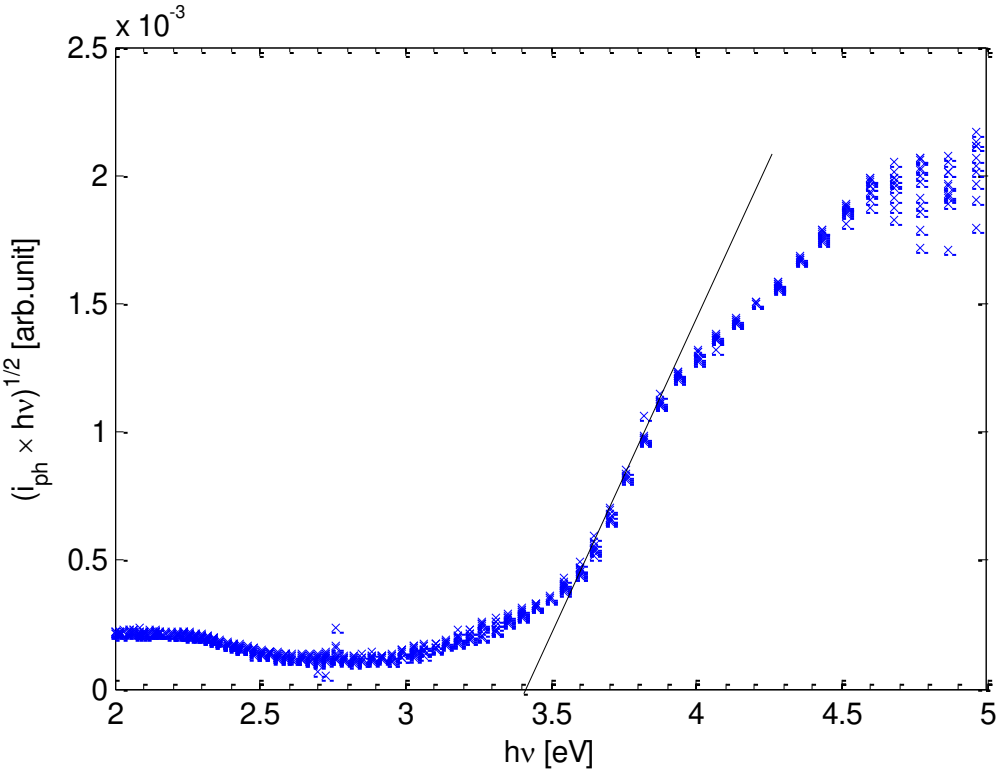

Figure 4.17 : Indirect bandgap for N500 on HOPG.

Whereas the N500 powder did not show any significant changes in photocurrent with respect to the undoped $CaNb_2O_6$, the N600 powder yielded a photocurrent in the visible region as shown in Figure 4.18. Interpretation of the photocurrent with respect to direct and indirect bandgaps was done for this measurement as well and yielded an indirect bandgap of 2.5eV, Figure 4.19. A direct bandgap was not determined as the plot for *n=1/2* did not yield a distinct linear region.

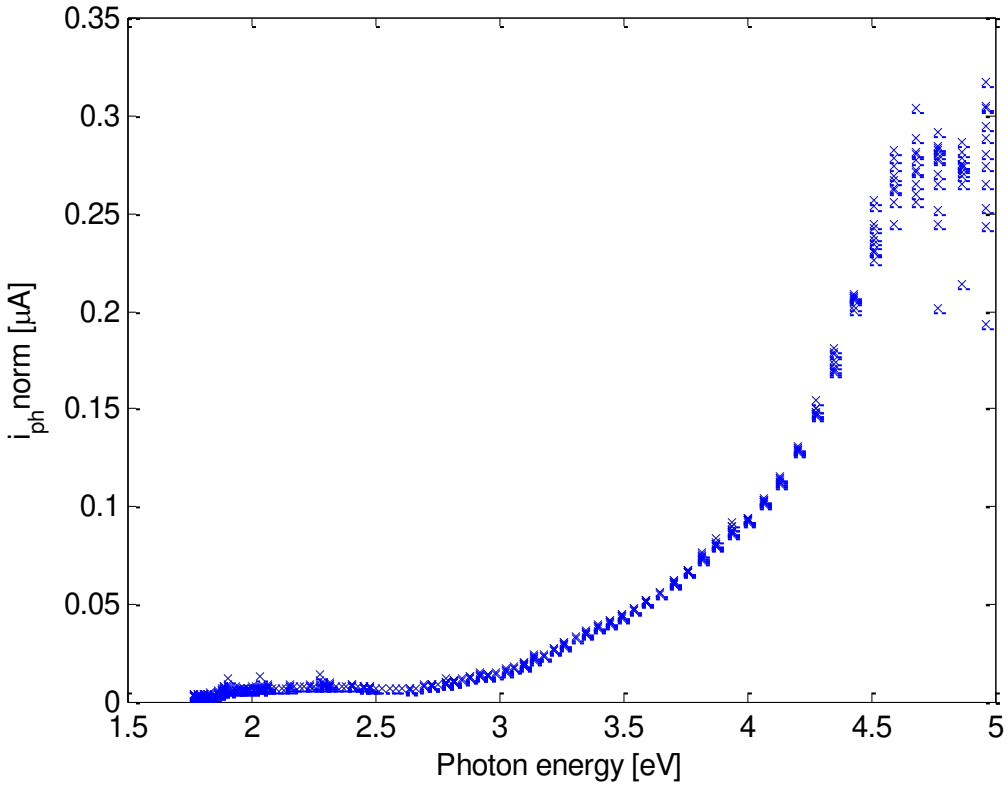

Figure 4.18 : Normalized photocurrent for N600 on GC polarized at 1.2V.

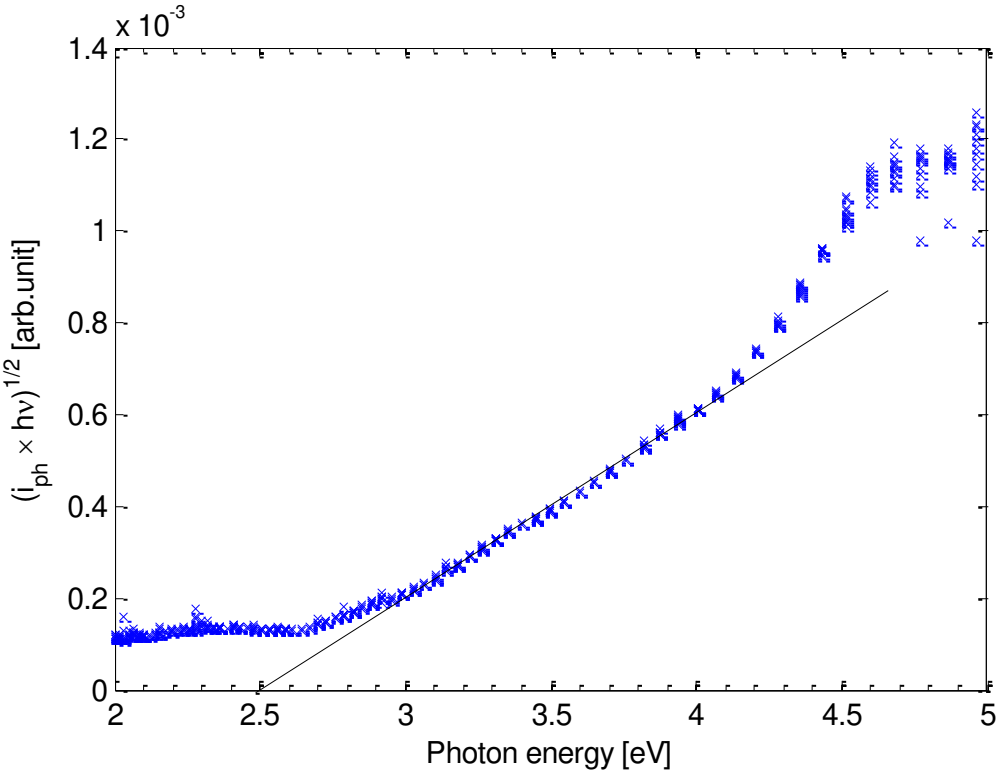

Figure 4.19 : Indirect bandgap for N600 on GC.

The effect of adding a hole scavenger to the electrolyte was investigated by adding approximately 9vol% concentrated acetic acid to the electrolyte. This resulted in a significant increase in photocurrent at high anodic potentials as illustrated for N500 in Figure 4.20. The curves in Figure 4.20 are not normalized with respect to intensities of the light as this makes it easier to compare the trends of the curves. Moreover the hole scavenger did not seem to affect the photocurrent in any other way than by increasing its already existing characteristics.

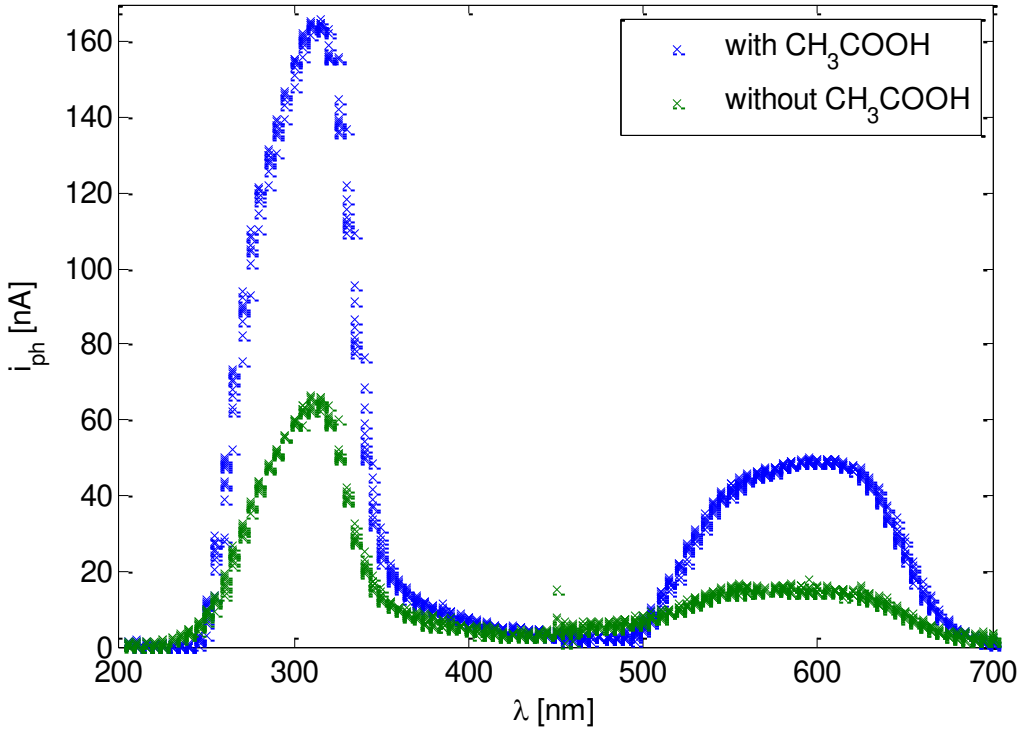

Figure 4.20 : Photocurrent of N500 both with and without the addition of concentrated acetic acid to the electrolyte.

4.4.3 Quasi-Fermi level measurements

Quasi-Fermi level measurements were done with the intention of determining the flatband potential of $CaNb_2O_6$ particles in a suspension. The measurements described in this section were performed by PhD candidate Morten Tjelta. Several experiments with $CaNb_2O_6$ suspensions in an electrolyte consisting of KNO_3 and acetic acid as hole scavenger were performed both with and without adding a Ru(III) complex as electron scavenger. However, none of the experiments produced any detectable photoresponse from the photocatalyst particles. Experiments with TiO_2 particles (Degussa P25) were therefore executed in order to validate the experimental procedure. By irradiating a suspension of TiO_2 particles with white light an anodic photocurrent that increased with time was observed, Figure 4.21.

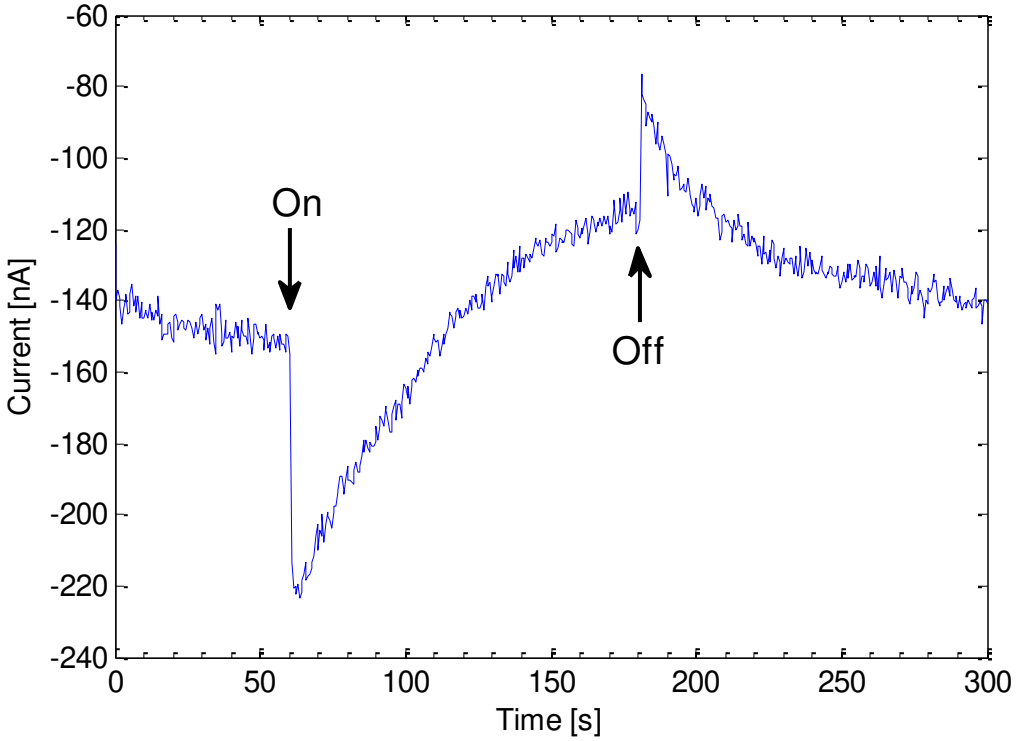

Figure 4.21 : White light irradiation of a suspension of TiO_2 particles in KNO_3 and acetic acid. The Pt working electrode was polarized at 700mV and the electrolyte was not stirred.

The light was turned on after 1 minute and a shift of the current in cathodic direction was observed before an increasing anodic photocurrent appeared. Similarly a shift in anodic direction resulted from turning off the light after 3 minutes before the cathodic current increased and approached the equilibrium value.

When the electrolyte was continuously stirred a saturated photocurrent of 800nm was measured after some minutes, Figure 4.22. This photocurrent was considerably larger than the photocurrent measured without stirring of the electrolyte. The stirring also increased the background noise of the measurements so that the shift from turning the light on and off was difficult to detect. By adding the Ru(III) complex to the suspension the photocurrent was further increased to 2.5µA after 2 minutes of irradiation with white light, Figure 4.23.

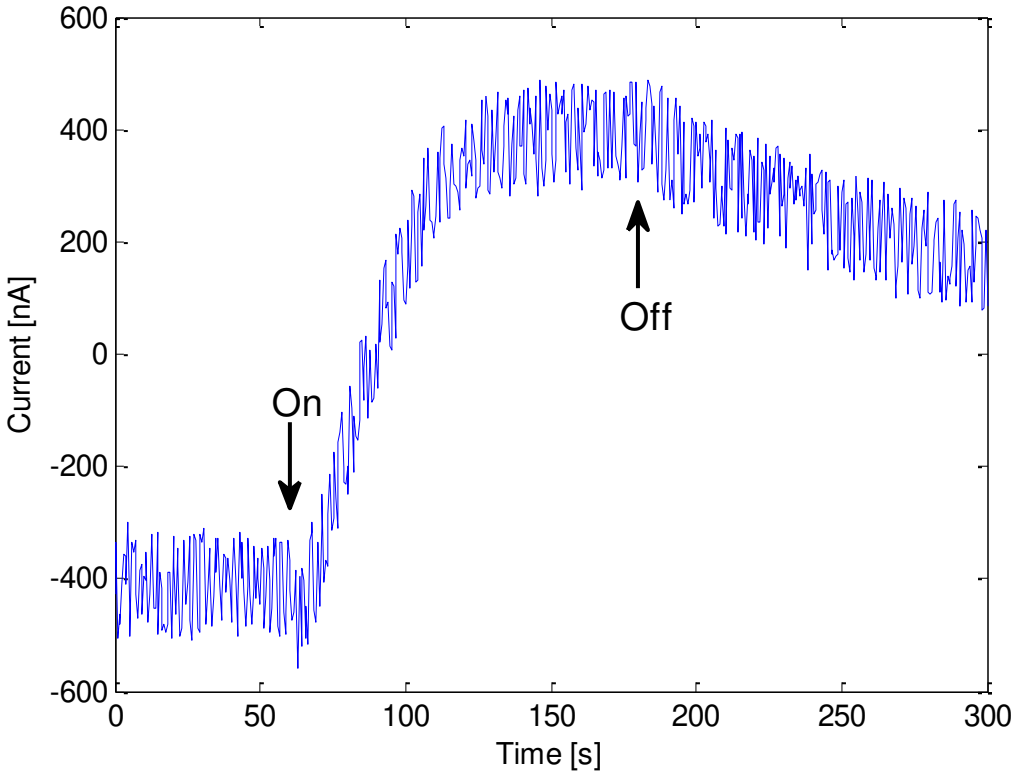

Figure 4.22 : White light irradiation of a stirred suspension of TiO_2 particles in KNO_3 and acetic acid. The Pt WE was polarized at 700mV.

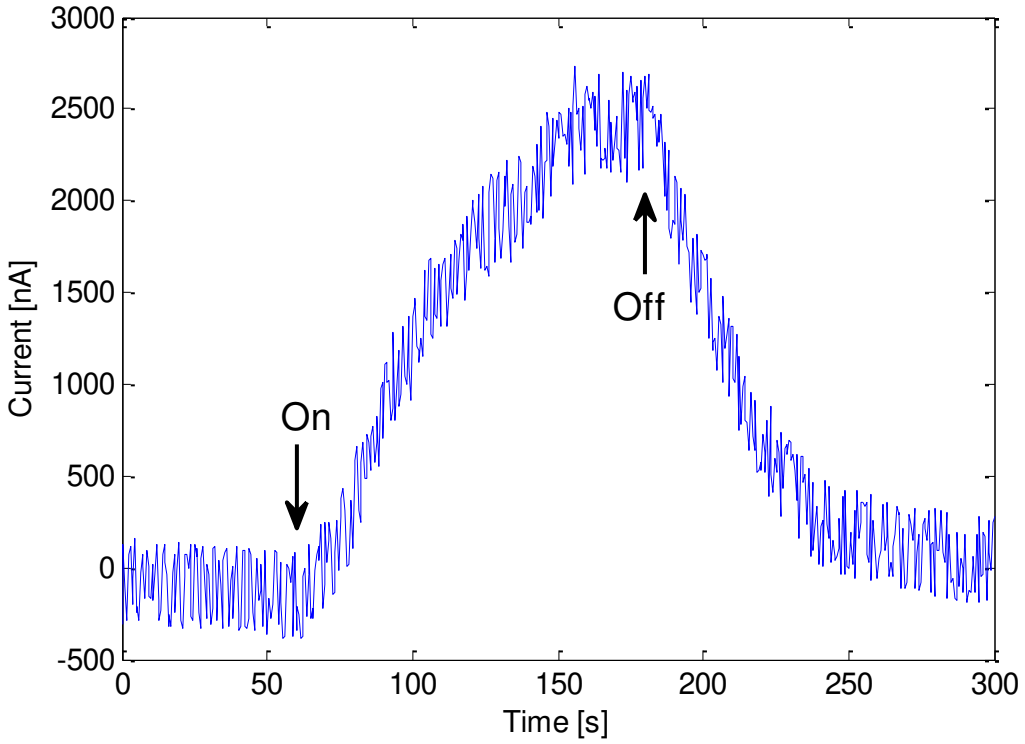

Figure 4.23 : White light irradiation of a stirred suspension of TiO_2 particles in KNO_3 and acetic acid with a Ru(III) complex added. Polarization of the Pt WE at 700mV.

4.5 Electrochemical impedance spectroscopy

For ideal electrochemical systems impedance could be used to obtain the capacitance of the space charge region in a semiconductor and hence determine its flatband potential, see section 2.4.5. Impedance measurements were performed on the electrode substrates both with and without a $CaNb_2O_6$ layer. The capacitance was calculated from high frequency measurements by modelling the system as the equivalent circuit in Figure 2.17 and using equation (2.46). Contributions from the Helmholtz capacitance were assumed to be negligible and the band edges of the photocatalyst considered as pinned for the measurements with the oxide. Hence the calculated capacitance should represent a Helmholtz capacitance for the electrode measurement and a space charge capacitance for the measurements on the $CaNb_2O_6$ powder.

It was discovered that the impedance of the measurements with and without the photocatalyst layer were quite similar and did not yield significant differences for the calculated capacitance. As a representative example the capacitance calculated at a frequency of 11kHz for a GC rotating disk electrode (RDE) both with and without $CaNb_2O_6$, Figure 4.24 and Figure 4.25 respectively, is shown below. The measurements were done by increasing the potential from 0V to 1.2V with steps of 50mV.

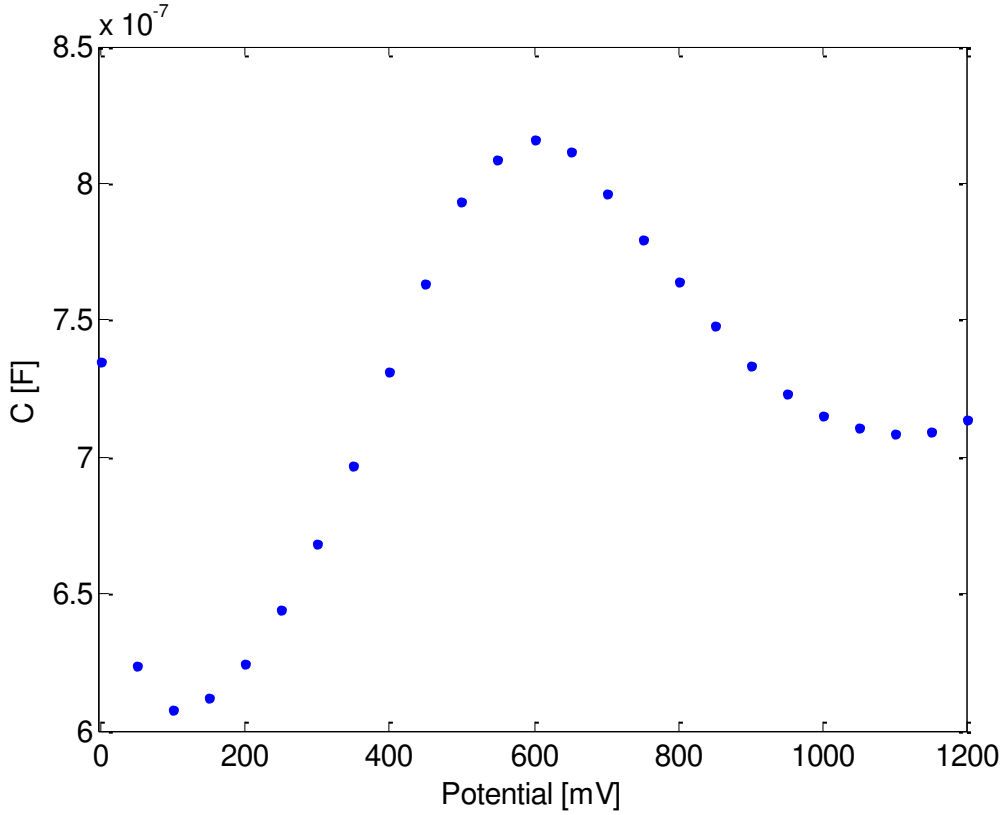

Figure 4.24 : Capacitance calculated at 11kHz for a GC RDE sprayed with $CaNb_2O_6$.

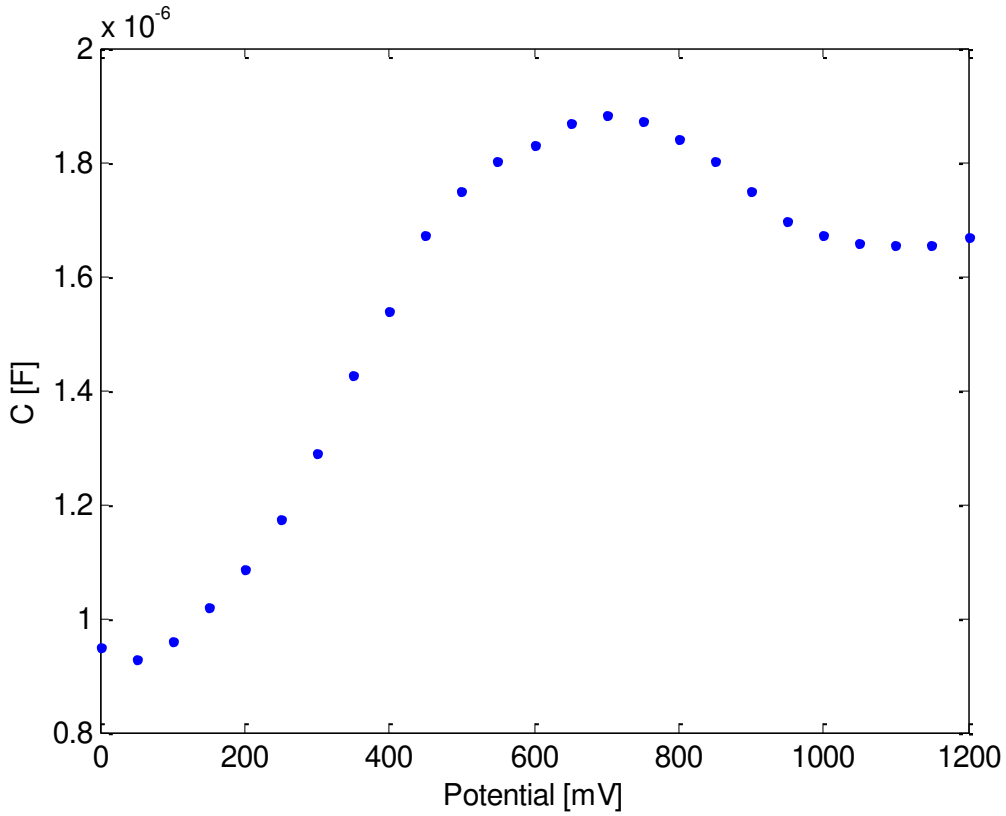

Figure 4.25 : Capacitance calculated at 11kHz for a GC RDE.

The capacitance calculated for the GC RDE was about 2 times larger than the capacitance calculated for the GC RDE with a thick layer of $CaNb_2O_6$ sprayed onto the surface. Both curves showed a similar dependence on potential with a peak in capacitance at 600-700mV. Because of the similar shape and size of the capacitance variation it seems like the measured capacitance could not solely be due to the space charge capacitance of the photocatalyst.

Therefore a theoretical consideration of the electrochemical system with respect to double-layer capacitances was done. Since the $CaNb_2O_6$ layer at the surface of the substrate is porous there will most likely be holes in the film where the substrate is exposed to the electrolyte. A Helmholtz capacitance, C_H, will then be associated with the exposed substrate. In addition there might be a capacitance associated with the photocatalyst-substrate interface, C_S, if the contact is not ohmic, but rather a Schottky junction. The possible capacitances present influencing the impedance measurements are illustrated in Figure 4.26.

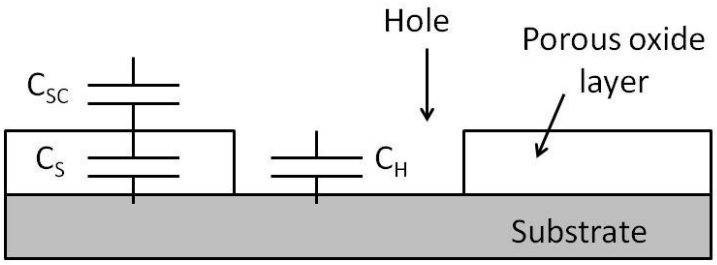

Figure 4.26 : The possible double layer capacitances associated with the electrode.

In the above figure the Helmholtz capacitance at the surface of the photocatalyst layer was neglected as it usually is considerably larger than the space charge capacitance. The total capacitance *C* when all the three capacitors shown in Figure 4.26 are present is given by:

$$C = C_H + \frac{1}{\frac{1}{C_{SC}} + \frac{1}{C_S}} \tag{3.1}$$

Hence the capacitance calculated from impedance measurements will strongly depend on the electrode surface and the contact between the photocatalyst and the substrate. In addition the presence of surface states can also affect the measured capacitance as described in section 2.1.4. This will be explained in more detail in the discussion.

5 Discussion

5.1 Doping with nitrogen

Doping of $CaNb_2O_6$ with nitrogen resulted in a color change of the powder from white for undoped $CaNb_2O_6$ via grey for the N500 and N600 powders to almost black for the powder doped at 700°C as shown in Figure 4.1. An increase in temperature yielded a darker color of the powder and thus seemed to enhance the doping efficiency and incorporate more nitrogen in the oxide. Similar color changes have been observed by amongst others Beranek and Kisch [39] for N-doped TiO_2 where the color changed from yellow to orange with increasing doping temperature. From elemental analysis they confirmed that an increased color corresponded to an increased doping of the oxide.

A shift of the absorption edge into the visible region was observed for the N500 sample from diffuse reflectance measurements, Figure 4.8. Furthermore the N600 and N700 samples showed increased absorption for all energies of the irradiating light. These measurements indicate that the electronic structure and the optical properties of the N-doped $CaNb_2O_6$ has been changed the most for the powder doped at the highest temperature. This supports the fact that a darker color imply more doping since a larger amount of nitrogen in the oxide would result in a more modified electronic structure. In addition photocurrent measurement showed a red-shift of the absorption edge for the N600 powder with respect to the undoped oxide, Figure 4.18, whereas no shift was found for the N500 sample. Correspondingly the electronic structure of N600 is probably altered more than the electronic structure of N500. A similar relation between the shift of the absorption edge and the amount of nitrogen doping has been observed by Cho et al. [15] for $CaNb_2O_6$ nanoplates.

Theoretical considerations using DFT calculations, Figure 4.3 and Figure 4.4, predicted that the oxygen lattice sites substituted with nitrogen would create isolated narrow energy bands above the VB. Such intermediate energy levels have also been described by Nakamura et al.[40] proposing that a narrow N 2p-band slightly above the VB was responsible for the visible light response of N-doped TiO_2. Subsequently absorption of light in the visible region should in theory be obtainable for N-doped $CaNb_2O_6$ as well. This was further confirmed by calculating the JDOS for pure and nitrogen doped $CaNb_2O_6$, Figure 4.5 and Figure 4.6 respectively, showing transition possibilities in the visible region for the N-doped oxide. The experimental measurements seemed to coincide well with the theory as absorption of light in the visible region was observed for both the N500 and N600 powders as already mentioned. Thus the red-shift of the absorption edge for N-doped $CaNb_2O_6$ could be explained by intermediate bands formed above the VB. Nevertheless it should be emphasized that the JDOS only predicts at what energies of light a transition could occur, but not to what extent it actually will occur.

When attributing the visible light absorption in N-doped $CaNb_2O_6$ to intermediate energy bands traditional methods for determining the bandgaps will not be applicable since several separate energy bands contribute to the measured light absorption. However, Asahi et al.[41] have reported on the basis of band structure calculations that visible-light responses for $TiO_{2-x}N_x$ arise from band narrowing by mixing of N-2p and O-2p orbitals. Cho et al.[15] also predicted from DFT calculations that N-doping of $CaNb_2O_6$ nanoplates would lead to a hybridization of N 2p and O 2p orbitals decreasing the bandgap. If this is the case for the N-doped $CaNb_2O_6$ powder investigated in this report a decrease in bandgap with nitrogen doping should be observable. Thus the diffuse reflectance data and the photocurrent measurements were used to estimate bandgaps from tangent lines in the *hv* vs. $(F(R_\infty)hv)^{1/n}$ and $(i_{ph}hv)^{1/n}$ plots respectively, see section 4.4.2. Both techniques showed a large decrease in the size of the bandgap for the N-doped $CaNb_2O_6$ compared to the undoped oxide. The bandgap of undoped $CaNb_2O_6$ was in accordance with both the value calculated from DFT and values reported in the literature [26, 42]. The bandgaps for N-doped samples also agreed with experimental values found by Cho et al.[15], but were smaller than their predicted value from DFT calculations. This could be explained by other factors contributing to the bandgap narrowing such as oxygen vacancies and chemisored nitrogen species at the surface as have been reported for N-doped TiO_2 [40].

Doping with nitrogen could lead to a transformation of the crystal structure of the oxide into e.g. an oxynitride if the proportion of substituted anions exceeded the tolerance of the oxide [10]. Such a transformation would induce significant changes to the electronic structure and absorption properties of the material. Because of the lower electronegativity of nitrogen with respect to oxygen the bandgaps in oxynitrides are smaller than in the related oxide [43] and will absorb light in the visible region. However, XRD scans of both pure and nitrogen doped powder, Figure 4.2, was identified as pure orthorhombic $CaNb_2O_6$. Additionally the formation of e.g. $CaNbO_2N$ from $CaNb_2O_6$ requires exposure to ammonia for periods much longer than 2h as used for the N-doping of $CaNb_2O_6$ [44]. For further investigations of the doping amounts and chemical nature of nitrogen species in the N-doped $CaNb_2O_6$ X-ray photoelectron spectroscopy should be applied. Also combustion analysis could be applied in order to determine the anion stoichiometry in the N-doped samples.

Several possible linear regions were observed in the bandgap plots from photocurrent measurements, and could be attributed to deep donor states as have been reported by Enache et al. [45]. Often these donor states are caused by oxygen vacancies in the lattice. In addition at high temperatures ammonia dissociates into N_2 and H_2 and the presence of H_2 may lead to a reduction of niobium into e.g. Nb^{3+} and Nb^{4+} which can act as electron-hole recombination centers [43, 44]. The equilibrium of the dissociation is however established slowly and can to some extent be suppressed using high flow rates and will thus limit the presence of the reduced niobium species.

5.2 Flatband potential

5.2.1 Electrochemical impedance spectroscopy

Impedance measurements were combined with theoretical considerations of double layer capacitances at the working electrode surface. In conclusion it appears that impedance measurements cannot be used to determine the space charge capacitance and hence the flatband potential of a porous photocatalyst layer on a conducting substrate. As described in section 4.5 parts of the substrate will always be exposed to the electrolyte due to pores in the oxide layer. A corresponding Helmholtz capacitance, C_H, will be present at the substrate surface and can be modeled as a capacitance in parallel with the space charge capacitance C_{SC}, see Figure 5.1. Additional capacitances due to the formation of a Schottky contact between the substrate and the photocatalyst, C_S, or the presence of surface states, C_{SS}, might also be present and modeled as capacitances in series with the space charge capacitance.

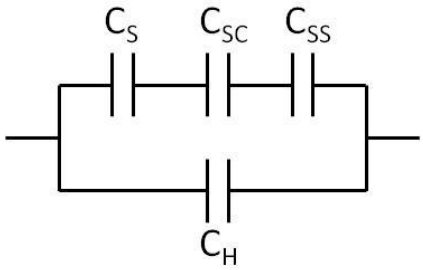

Figure 5.1 : Equivalent circuit showing possible double layer capacitances associated with the substrate-photocatalyst-electrolyte interfaces.

The capacitance extracted from impedance measurements will be composed of contributions from all the capacitances shown in Figure 5.1. Since the Helmholtz layer usually is much smaller compared to the space charge region in a semiconductor, the Helmholtz capacitance will be much larger than the space charge capacitance. Equation (5.1) shows that the capacitance associated with the space charge region will be negligible compared to the Helmholtz capacitance for the substrate.

$$C = C_H + \frac{1}{\frac{1}{C_{SC}} + \frac{1}{C_S} + \frac{1}{C_{SS}}} \tag{5.1}$$

Thus the capacitance calculated from impedance measurements will only reflect the capacitance of the substrate. This appeared to be the case for a $CaNb_2O_6$ layer on glassy carbon. The capacitances measured for the substrate both with and without the oxide layer were similar in both shape and size, Figure 4.24 and Figure 4.25 respectively. In order to

determine the flatband potential of a photocatalyst layer using impedance the substrate need to be completely covered and no pinholes should be present in the oxide layer.

When the requirement of a completely dense layer of the photocatalyst is fulfilled the presence of a Schottky contact or surface states may still affect the measured capacitance. If the space charge capacitance is large compared to the capacitance of a Schottky junction or surface states these will dominate the measurement instead of the space charge capacitance. This has been observed by Klahr et al.[46] when illuminating pinholefree layers of Fe_2O_3. The resulting capacitance vs. potential plots revealed that surface states dominated the measurements. Since the shape of the capacitance vs. potential plots in this report also resembles the theoretical curve for a surface state capacitance described in section 2.1.4 it might seem like surface states are present at 600mV with respect to the reference electrode. However as these states also are present in the curve without a $CaNb_2O_6$ layer at the surface they should be attributed to energy states at the substrate surface and not the photocatalyst surface.

In brief a dense, pinholefree photocatalyst layer creating an ohmic contact with the substrate is required to measure the space charge capacitance and hence the flatband potential of a semiconductor oxide from impedance measurements. However several reports in the literature [47, 48] describe the determination of the flatband potential of mesoporous oxide layers by using complicated equivalent circuits, EIS, and Mott-Schottky plots. The application of EIS for porous oxide layers might therefore be possible if reliable equivalent circuits for the electrochemical system are developed and applied in the impedance investigations.

5.2.2 Quasi-Fermi level measurements

In the quasi-Fermi level measurements $CaNb_2O_6$ did not yield any measurable photocurrent and does not appear to be very reactive in suspension. At the same time TiO_2 yielded a clear photocurrent that depended on both stirring of the suspension and the addition of a Ru(III) complex as electron scavenger. This confirmed that the experimental setup functioned as intended.

An anodic photocurrent was observed for TiO_2 with a transient current response for the measurement without stirring of the suspension, Figure 4.21. The negative current transients upon turning the light on could be due to particles close to or at the surface of the Pt working electrode. When these particles are illuminated electron-hole pairs are generated, and since holes will be collected by the hole scavenger the electrons can be trapped in e.g. surface states creating an cathodic current transient. After filling the trap states the electrons will contribute to the diffusion limited anodic photocurrent.

When stirring the suspension of TiO_2 particles the photocurrent increased considerably, Figure 4.22. Since the photocurrent was detected at the Pt working electrode it will be limited by the diffusion of reduced species or charged particles to the electrode surface. Consequently

when the suspension was stirred more particles and reduced species would reach the Pt electrode and transfer the photoexcited electrons. Furthermore the photocurrent was additionally enhanced when adding an electron scavenger (Ru(III) complex) to the suspension, Figure 4.23. This indicates that the electron scavenger functioned as intended and efficiently collected electrons created by excitation in the semiconductor particles and transferred them to the Pt electrode. It could also be noted that the photocurrent decay when turning off the light was faster with an electron scavenger present indicating more efficient charge transfer processes.

Photocurrent measurements on porous $CaNb_2O_6$ electrodes confirmed the efficiency of adding CH_3COOH as a hole scavenger to the electrolyte as the measured photocurrent increased considerably, Figure 4.20. This indicates that the transfer of holes from the porous semiconductor layer to the electrolyte is slow and kinetically limited, but could to some extent be overcome by adding a suitable hole scavenger to the electrolyte. The presence of acetic acid as a hole scavenger in the $CaNb_2O_6$ suspensions should therefore eliminate photocurrent limitations due to hole transfer kinetics. Nevertheless no photocurrent from the $CaNb_2O_6$ suspensions was detectable. This could be explained by the difference in pH of the electrolyte used for measurements on the porous electrodes and the suspension. The porous electrodes were investigated in 0.5M H_2SO_4 yielding a pH of approximately 0. On the other hand the support electrolyte in the suspension measurements was 0.5M KNO_3 and the pH was approximately 6. Since the PZC of $CaNb_2O_6$ have experimentally been determined as 3, the surface of the $CaNb_2O_6$ particles would go from positive to negative by increasing the pH from 0 to 6. Correspondingly the band edges would in theory be shifted upwards on the electrochemical scale with 59mV per pH unit. If the redox potential of acetic acid could be regarded as independent of pH the overlap between the valence band edge of the semiconductor and the Gaussian distribution of the hole scavenger would be altered and could result in a reduced hole current.

Furthermore the addition of the Ru(III) complex as an electron scavenger to the $CaNb_2O_6$ suspensions still did not yield any measurable photocurrent all though it was found to efficiently enhance the photocurrent in the TiO_2 suspensions. An explanation for this could be the position of the conduction band edge in $CaNb_2O_6$. The flatband potential of $CaNb_2O_6$ has only been determined by theoretical approaches and by assuming that the Fermi level of the electrons was approximately at the same position as the conduction band edge. Since the two different Mulliken electronegativities used in the calculations yielded quite different flatband potentials, Figure 4.7, the accurate position of the conduction band edge is not known. If the conduction band edge is situated at more positive energies than the redox potential of the electron scavenger the photogenerated electrons will not possess enough energy to reduce the Ru(III) complex. Thus the electron scavenger would not enhance the photocurrent.

The position of both the valence and conduction band edge with respect to the scavenger redox potentials seems to be of great importance for the detection of a photocurrent in $CaNb_2O_6$ suspensions as has been discussed in section 2.4.2. In order to obtain a photocurrent from $CaNb_2O_6$ particles in suspension the pH of the suspension should be changed. A higher

pH will shift the energy bands of $CaNb_2O_6$ to even more negative potentials and could result in a larger overlap between the CB and the DOS of the electron scavenger. Similarly a better overlap between the VB and the DOS of the hole scavenger could be obtained by reducing the pH. It should be emphasized however that this requires that the scavenger redox potentials do not depend on pH.

The lack of a measurable photocurrent from the $CaNb_2O_6$ suspensions could also be attributed to recombination of the charge carriers. If the lifetime of the charge carriers in $CaNb_2O_6$ is low the corresponding diffusion length will be short. Thus the charge carriers might recombine before they reach the electrolyte. A high concentration of defects such as oxygen vacancies will lower the diffusion length by enhancing recombination. This could be further investigated by performing flash photolysis and examine the resulting photocurrent transients. Also slow charge transfer kinetics would enhance the recombination of the charge carriers as they would accumulate in the particles. The $CaNb_2O_6$ particles used in the experiments should be as small as possible in order to reduce recombination and enhance charge transfer to the electrolyte.

5.3 Photocurrent transients

The photocurrent rise time in the porous $CaNb_2O_6$ electrodes was quite long as can be seen from Figure 4.12. A possible explanation for the increase in photocurrent over time could be attributed to photocorrosion of the oxide. When electron-hole pairs are generated by light under depletion conditions the quasi-Fermi level of holes at the surface will be different from the Fermi level in the bulk. The holes may then possess sufficient energy to oxidize the photocatalyst. The general form of this anodic decomposition reaction of an oxide can be written as:

$$M_xO_y + \frac{2y}{x}h^+ \rightleftharpoons xM_{(aq)}^{(2y/x)+} + \frac{y}{2}O_2 \tag{5.2}$$

Whether or not this undesired reaction occurs depends on the position of the redox potential for the anodic decomposition, $E_{p,decomp}$, with respect to the quasi-Fermi level of the holes. If the potential is below the valence band edge no anodic decomposition can occur. The addition of a suitable co-catalyst favoring the water oxidation could alleviate the anodic decomposition of the oxide to some extent. Also the anodic decomposition could be reduced by adding a suitable hole scavenger to the electrolyte. However the addition of acetic acid to the electrolyte did not eliminate the photocurrent transients of the porous $CaNb_2O_6$ electrodes and suggests that the transients were governed by other processes.

In microporous oxide films the colloids will be surrounded by electrolyte and band bending can thus be negligible. The separation of photogenerated charge carriers will then be determined by the efficiency of electron and hole transfer at the semiconductor-electrolyte and semiconductor-substrate interfaces. If the photoexcited hole is collected by a hole

acceptor in the electrolyte the photocurrent will be limited by the diffusion of electrons through the porous film. This means that the electrons can recombine with e.g. an electron acceptor all the way to the back contact. In addition if the contact between the oxide film and the substrate is not ohmic the electrons are doomed to recombine. Södergren et al. [49] have developed models for the action spectra and I-V characteristics of microporous semiconductor film electrodes under illumination. This was achieved by solving the diffusion equation described in section 2.1.5 by assuming that the electron transport in the microporous semiconductor material to the back contact occurred via diffusion, and that the diffusion length of the electrons in the semiconductor was constant. More recent studies [50] have investigated different models for diffusional charge transport in microporous films and obtained theoretical time dependent photocurrents with shapes similar to the ones observed in porous $CaNb_2O_6$ films. As a consequence the photocurrent transients could be attributed to the diffusion of electrons to the back contact.

5.4 $CaNb_2O_6$ as a photocatalyst in water splitting

Main requirements for a photocatalyst to be used in water splitting is good visible light absorption, favorable band edge positions, high photochemical stability, high catalytic activity and fast and efficient charge transport.

The bandgap of undoped $CaNb_2O_6$ is too large to achieve visible light absorption. From theoretical calculations of the flatband potential and the bandgap of $CaNb_2O_6$, section 4.2, it was found that E_C will be only slightly more negative than the reduction potential of protons while E_V will be significantly positive with respect to the oxidation of H_2O. Therefore modification of the valence band seemed to be the best approach in order to narrow the bandgap of $CaNb_2O_6$ and extend the absorption of light into the visible region. A raise of the valence band maximum could be achieved by introducing anions such as nitrogen, carbon and sulfur on the O sites of the oxide as described by Tong et al.[10]. This appeared to be the case for nitrogen doping of $CaNb_2O_6$ since the absorption edge was shifted towards lower photon energies compared to the undoped oxide. Nevertheless the bandgap of the N-doped photocatalyst still seems to be too large to be applied as a photocatalyst in water splitting since the ideal bandgap of a photocatalyst used in water splitting would be around 2.2eV [16].

What's more the measured photocurrents of $CaNb_2O_6$ were quite low and often not detectable indicating a low incident photon to current conversion efficiency. This could be attributed to high recombination rates due to slow charge transport in the oxide and slow charge transfer kinetics between the oxide and the electrolyte. For the porous electrodes the existence of a Schottky junction rather than an ohmic contact with the electrode substrate would also induce recombination by accumulation of electrons at the interface. Furthermore a high concentration of defects could be present in the oxide and would together with surface states enhance the recombination rates.

5.5 Further work

In order to obtain a complete understanding on how nitrogen doping affects the band structure of $CaNb_2O_6$ further investigations are needed. The N-doped oxide should be examined using XPS and combustion analysis to determine the amount of oxygen substituted by nitrogen in the photocatalyst. Besides XPS analysis could yield information on the chemical nature of nitrogen species in N-doped $CaNb_2O_6$. This information will be indispensable for optimizing the nitrogen doping of $CaNb_2O_6$ by e.g. changing the nitridation temperature and flow rates of ammonia. Also further investigations on doping could be done by doping $CaNb_2O_6$ with other anions such as carbon and sulphur and see if they yield results similar to the N-doping.

The measured photocurrent of $CaNb_2O_6$ is low. If $CaNb_2O_6$ is to be employed as a photocatalyst the efficiency need to be drastically increased and thus the reason for the low photon to current efficiency should be exploited. One way of identifying recombination in the oxide is by applying flash photolysis [12]. A pulse laser is then used to excite electrons in the photocatalyst and the corresponding absorption spectrum of a transient and its decay with time is observed. Kinetic studies of the oxidation reactions at the surface of the oxide could be done by using a rotating ring disk electrode. The products formed at the semiconductor disk are then detected electrochemically at a noble metal ring and photocorrosion of $CaNb_2O_6$ could be identified. A characterization method for identifying the position of surface states that could lead to surface recombination is scanning tunnelling spectroscopy.

Other methods for electrode preparation should be investigated as the electrode properties have proven to affect the characterization and efficiency of the photocatalyst considerably. If pinhole free layers of $CaNb_2O_6$ could be produced, impedance measurements would be possible to employ in the determination of the flatband potential. Moreover by controlling the oxide layer thickness it could be tailored to match the thickness of the absorption coefficient of $CaNb_2O_6$ and improve the efficiency. Finally the photocatalytic activity of $CaNb_2O_6$ in an aqueous electrolyte under visible light irradiation could be tested by measuring the degradation of e.g. methylene blue [51].

6 Conclusion

Experimental techniques were combined with theoretical approaches to determine the electronic structure of pure and nitrogen doped $CaNb_2O_6$. The material showed photocatalytic activity upon illumination and doping with nitrogen shifted the absorption edge of the oxide into the visible light region. From DFT calculations the shift was attributed to the formation of narrow energy bands above the valence band of pure $CaNb_2O_6$. An alternative explanation suggested a hybridization of N 2p and O 2p bands and a corresponding decrease in the size of the bandgap with respect to the undoped oxide was observed. X-ray diffraction confirmed phase pure orthorhombic $CaNb_2O_6$ for both pure and N-doped oxide and excluded the possible transformation of the oxide into e.g. an oxynitride.

Impedance measurements were found to be dominated by the electrode substrate and it was concluded that a pinhole-free oxide layer creating an ohmic contact with the substrate is required to measure the space charge capacitance. Low photocatalytic activities of $CaNb_2O_6$ in suspension suggested limitations due to low conductivity, high concentrations of recombination centers or slow charge transfer kinetics. The latter was confirmed for porous oxide layers as the addition of a hole scavenger increased the measured photocurrent. Positive photocurrent transients were observed for $CaNb_2O_6$ and could be related to diffusion of electrons through the porous oxide film or by photanodic decomposition of the photocatalyst.

From theoretical considerations $CaNb_2O_6$ seems to possess band edge positions favorable for water splitting. Additionally a reduction of the bandgap and visible light absorption was obtained by doping with nitrogen. However in order to use $CaNb_2O_6$ as a photocatalyst for water splitting the bandgap needs to be further decreased. Also the photon to current efficiency should be considerably increased and requires further investigations of the charge transport and kinetic limitations of the oxide.

7 References

1. Lewis, N.S. and D.G. Nocera, *Powering the planet: Chemical challenges in solar energy utilization.* Proceedings of the National Academy of Sciences, 2006. **103**(43): p. 15729-15735.

2. *Basic research needs for solar energy utilization*, 2005, US Department of energy, Office of Basic Energy Sciences.

3. van de Krol, R., Y. Liang, and J. Schoonman, *Solar hydrogen production with nanostructured metal oxides.* Journal of Materials Chemistry, 2008. **18**(20): p. 2311-2320.

4. Fujishima, A. and K. Honda, *Electrochemical Photolysis of Water at a Semiconductor Electrode.* Nature, 1972. **238**(5358): p. 37-38.

5. Minggu, L.J., W.R. Wan Daud, and M.B. Kassim, *An overview of photocells and photoreactors for photoelectrochemical water splitting.* International Journal of Hydrogen Energy, 2010. **35**(11): p. 5233-5244.

6. Abe, R., *Recent progress on photocatalytic and photoelectrochemical water splitting under visible light irradiation.* Journal of Photochemistry and Photobiology C: Photochemistry Reviews, 2010. **11**(4): p. 179-209.

7. Maeda, K., *Photocatalytic water splitting using semiconductor particles: History and recent developments.* Journal of Photochemistry and Photobiology C: Photochemistry Reviews, 2011(0).

8. Kudo, A. and Y. Miseki, *Heterogeneous photocatalyst materials for water splitting.* Chemical Society Reviews, 2009. **38**(1): p. 253-278.

9. Kudo, A., *Recent progress in the development of visible light-driven powdered photocatalysts for water splitting.* International Journal of Hydrogen Energy, 2007. **32**(14): p. 2673-2678.

10. Tong, H., et al., *Nano-photocatalytic Materials: Possibilities and Challenges.* Advanced Materials, 2012. **24**(2): p. 229-251.

11. Bard, A.J., M. Stratmann, and S. Licht, *Semiconductor Electrodes and Photoelectrochemistry*. Encyclopedia of Electrochemistry. Vol. 6. 2002: Wiley-VCH Verlag GmbH.

12. Memming, R., *Semiconductor Electrochemistry*, 2001, Weinheim, Germany: Wiley-VCH Verlag GmbH.

13. van den Meerakker, J.E.A.M., E.A. Meulenkamp, and M. Scholten, *(Photo)electrochemical characterization of tin-doped indium oxide.* Journal of Applied Physics, 1993. **74**(5): p. 3282-3288.

14. Beranek, R., *(Photo)electrochemical Methods for the Determination of the Band Edge Positions of TiO_2-Based Nanomaterials.* Advances in Physical Chemistry, 2011. **2011**.

15. Cho, I.-S., et al., *Preparation of N-Doped $CaNb_2O_6$ Nanoplates with Ellipsoid-Like Morphology and Their Photocatalytic Activities Under Visible-Light Irradiation.* Journal of Nanoscience and Nanotechnology, 2010. **10**(2): p. 1196-1202.

16. van de Krol, R. and M. Grätzel, *Photoelectrochemical Hydrogen Production*. 1 ed. Electronic Materials: Science and Technology. Vol. 102. 2012: Springer.

17. Kittel, C., *Introduction to Solid State Physics*. 8th ed2005: John Wiley & Sons.

18. Bard, A.J., R. Memming, and B. Miller, *Terminology in Semiconductor Electrochemistry and Photoelectrochemical Energy Conversion (Recommendations 1991).* Pure and Applied Chemistry, 1991. **63**(4): p. 569-596.

19. Nozik, A.J. and R. Memming, *Physical Chemistry of Semiconductor−Liquid Interfaces.* The Journal of Physical Chemistry, 1996. **100**(31): p. 13061-13078.

20. Gerischer, H., *Charge transfer processes at semiconductor-electrolyte interfaces in connection with problems of catalysis.* Surface Science, 1969. **18**(1): p. 97-122.

21. Hamann, C.H., A. Hamnett, and W. Vielstich, *Electrochemistry*. 2. ed, 2007, Weinheim: Wiley-VCH Verlag GmbH.

22. Dotan, H., et al., *Probing the photoelectrochemical properties of hematite (α-Fe_2O_3) electrodes using hydrogen peroxide as a hole scavenger.* Energy & Environmental Science, 2011. **4**(3): p. 958-964.

23. Butler, M.A. and D.S. Ginley, *Principles of photoelectrochemical, solar energy conversion.* Journal of Materials Science, 1980. **15**(1): p. 1-19.

24. Roy, A.M., et al., *Determination of the flatband potential of semiconductor particles in suspension by photovoltage measurement.* International Journal of Hydrogen Energy, 1995. **20**(8): p. 627-630.

25. Hagfeldt, A., U. Björkstén, and M. Grätzel, *Photocapacitance of Nanocrystalline Oxide Semiconductor Films: Band-Edge Movement in Mesoporous TiO_2 Electrodes during UV Illumination.* The Journal of Physical Chemistry, 1996. **100**(20): p. 8045-8048.

26. Cho, I.-S., et al., *Effects of crystal and electronic structures of ANb_2O_6 (A=Ca, Sr, Ba) metaniobate compounds on their photocatalytic H_2 evolution from pure water.* International Journal of Hydrogen Energy, 2010. **35**(23): p. 12954-12960.

27. Harrison, W.A., *Electronic structure and the properties of solids: the physics of the chemical bond*. 2 ed, 1989: Dover Publications.

28. Putz, M.V., N. Russo, and E. Sicilia, *About the Mulliken electronegativity in DFT.* Theoretical Chemistry Accounts: Theory, Computation, and Modeling (Theoretica Chimica Acta), 2005. **114**(1): p. 38-45.

29. Gärtner, W.W., *Depletion-Layer Photoeffects in Semiconductors.* Physical Review, 1959. **116**(1): p. 84-87.

30. Ward, M.D. and A.J. Bard, *Photocurrent enhancement via trapping of photogenerated electrons of titanium dioxide particles.* The Journal of Physical Chemistry, 1982. **86**(18): p. 3599-3605.

31. Ward, M.D., J.R. White, and A.J. Bard, *Electrochemical investigation of the energetics of particulate titanium dioxide photocatalysts. The methyl viologen-acetate system.* Journal of the American Chemical Society, 1983. **105**(1): p. 27-31.

32. Hykaway, N., et al., *Current-doubling reactions on titanium dioxide photoanodes.* The Journal of Physical Chemistry, 1986. **90**(25): p. 6663-6667.

33. Torrent, J. and V. Barrón, *Diffuse Reflectance Spectroscopy*, in *Methods of Soil Analysis. Part 5 - Mineralogical Methods*, A.L. Ulery and L.R. Drees, Editors. 2008, Soil Science Society of America, Inc.: Madison, Wisconsin, USA.

34. Kubelka, P. and F. Munk, *Ein beitrag zur optik der farbanstriche.* Z. Tech. Phys., 1931. **12**: p. 593-601.

35. Morales, A.E., E.S. Mora, and U. Pal, *Use of diffuse reflectance spectroscopy for optical characterization of un-supported nanostructures.* Revista Mexicana de Física, 2007. **53**(5): p. 18-22.

36. Sluyters-Rehback, M., *Impedances of Electrochemical Systems: Terminology, Nomenclature and Representation - Part I: Cells with Metal Electrodes and liquid solutions (IUPAC Recommendations 1994).* Pure and Applied Chemistry, 1994. **66**(9): p. 1831-1891.

37. Tjelta, M., *PhD thesis to be published*, in *Department of Materials Science and Engineering*, Norwegian University of Science and Technology.

38. Buan, M.E.M., *Photoelectrochemical production of hydrogen*, in *Department of Materials Science and Engineering*2011, Norwegian University of Science and Technology.

39. Beranek, R. and H. Kisch, *Tuning the optical and photoelectrochemical properties of surface-modified TiO_2.* Photochemical & Photobiological Sciences, 2008. **7**(1): p. 40-48.

40. Nakamura, R., T. Tanaka, and Y. Nakato, *Mechanism for Visible Light Responses in Anodic Photocurrents at N-Doped TiO_2 Film Electrodes.* The Journal of Physical Chemistry B, 2004. **108**(30): p. 10617-10620.

41. Asahi, R., et al., *Visible-Light Photocatalysis in Nitrogen-Doped Titanium Oxides.* Science, 2001. **293**(5528): p. 269-271.

42. Cho, I.-S., et al., *Preparation, Characterization, and Photocatalytic Properties of $CaNb_2O_6$ Nanoparticles.* Journal of the American Ceramic Society, 2009. **92**(2): p. 506-510.

43. Fuertes, A., *Chemistry and applications of oxynitride perovskites.* Journal of Materials Chemistry, 2012. **22**(8): p. 3293-3299.

44. Siritanaratkul, B., et al., *Synthesis and Photocatalytic Activity of Perovskite Niobium Oxynitrides with Wide Visible-Light Absorption Bands.* ChemSusChem, 2011. **4**(1): p. 74-78.

45. Enache, C.S., et al., *Photo-electrochemical Properties of Thin-Film $InVO_4$ Photoanodes: the Role of Deep Donor States.* The Journal of Physical Chemistry C, 2009. **113**(44): p. 19351-19360.

46. Klahr, B., et al., *Water Oxidation at Hematite Photoelectrodes: The Role of Surface States.* Journal of the American Chemical Society, 2012. **134**(9): p. 4294-4302.

47. Baram, N. and Y. Ein-Eli, *Electrochemical Impedance Spectroscopy of Porous TiO_2 for Photocatalytic Applications.* The Journal of Physical Chemistry C, 2010. **114**(21): p. 9781-9790.

48. Wolcott, A., et al., *Photoelectrochemical Study of Nanostructured ZnO Thin Films for Hydrogen Generation from Water Splitting.* Advanced Functional Materials, 2009. **19**(12): p. 1849-1856.

49. Soedergren, S., et al., *Theoretical Models for the Action Spectrum and the Current-Voltage Characteristics of Microporous Semiconductor Films in Photoelectrochemical Cells.* The Journal of Physical Chemistry, 1994. **98**(21): p. 5552-5556.

50. Nissfolk, J., et al., *Interpretation of small-modulation photocurrent transients in dye-sensitized solar cells – A film thickness study.* Journal of Electroanalytical Chemistry, 2010. **646**(1–2): p. 91-99.

51. Jiang, H., M. Nagai, and K. Kobayashi, *Enhanced photocatalytic activity for degradation of methylene blue over V_2O_5/$BiVO_4$ composite.* Journal of Alloys and Compounds, 2009. **479**(1–2): p. 821-827.